Connecting the cosmic web to the spin of dark haloes: implications for galaxy formation

Sandrine Codis, Christophe Pichon, Julien Devriendt, Adrianne Slyz, Dmitry Pogosyan, Yohan Dubois, Thierry Sousbie

Monthly Notices
of the
ROYAL ASTRONOMICAL SOCIETY

Mon. Not. R. Astron. Soc. **427,** 3320–3336 (2012) doi:10.1111/j.1365-2966.2012.21636.x

Connecting the cosmic web to the spin of dark haloes: implications for galaxy formation

Sandrine Codis,[1] Christophe Pichon,[1,2]★ Julien Devriendt,[2] Adrianne Slyz,[2] Dmitry Pogosyan,[3] Yohan Dubois[1] and Thierry Sousbie[1]

[1]*Institut d'Astrophysique de Paris, 98 bis boulevard Arago, 75014 Paris, France*
[2]*Sub-department of Astrophysics, Department of Physics, University of Oxford, Keble Road, Oxford OX1 3RH*
[3]*Department of Physics, University of Alberta, 11322-89 Avenue, Edmonton, Alberta T6G 2G7, Canada*

Accepted 2012 June 28. Received 2012 April 27; in original form 2012 January 27

ABSTRACT

We investigate the alignment of the spin of dark matter haloes relative (i) to the surrounding large-scale filamentary structure, and (ii) to the tidal tensor eigenvectors using the Horizon 4π dark matter simulation which resolves over 43 million dark matter haloes at redshift zero. We detect a clear mass transition: the spin of dark matter haloes above a critical mass $M_0^{\rm s} \approx 5(\pm1) \times 10^{12}\,{\rm M}_\odot$ tends to be perpendicular to the closest large-scale filament (with an excess probability of up to 12 per cent), and aligned with the intermediate axis of the tidal tensor (with an excess probability of up to 40 per cent), whereas the spin of low-mass haloes is more likely to be aligned with the closest filament (with an excess probability of up to 15 per cent). Furthermore, this critical mass is redshift-dependent, scaling as $M^{\rm s}_{\rm crit}(z) \approx M^{\rm s}_0(1+z)^{-\gamma_{\rm s}}$ with $\gamma_{\rm s} = 2.5 \pm 0.2$. A similar fit for the redshift evolution of the tidal tensor transition mass yields $M^{\rm t}_0 \approx 8(\pm2) \times 10^{12}\,{\rm M}_\odot$ and $\gamma_{\rm t} = 3 \pm 0.3$. This critical mass also varies weakly with the scale defining filaments.

We propose an interpretation of this signal in terms of large-scale cosmic flows. In this picture, most low-mass haloes are formed through the winding of flows embedded in misaligned walls; hence, they acquire a spin parallel to the axis of the resulting filaments forming at the intersection of these walls. On the other hand, more massive haloes are typically the products of later mergers along such filaments, and thus they acquire a spin perpendicular to this direction when their orbital angular momentum is converted into spin. We show that this scenario is consistent with both measured excess probabilities of alignment with respect to the eigendirections of the tidal tensor, and halo merger histories. On a more qualitative level, it also seems compatible with 3D visualization of the structure of the cosmic web as traced by 'smoothed' dark matter simulations or gas tracer particles. Finally, it provides extra support to the disc-forming paradigm presented by Pichon et al. as it extends it by characterizing the geometry of secondary infall at high redshift.

Key words: methods: numerical – galaxies: formation – galaxies: haloes – large-scale structure of Universe.

1 INTRODUCTION

Over the past decades, numerical simulations and large redshift surveys have highlighted the large-scale structure (LSS) of our Universe, a cosmic web formed by voids, sheets, elongated filaments and clusters at their nodes (Bond, Kofman & Pogosyan 1996). This structure is believed to be the result of the linear growth of primordial Gaussian fluctuations in a nearly homogeneous density field followed by the non-linear collapse of overdense regions into dark matter (DM) haloes which then accrete mass and merge as described by the hierarchical model. The current paradigm of galaxy formation states that collapsing protogalaxies acquire their spin (i.e. their angular momentum) by tidal torquing because of a misalignment between their inertia tensor and the local gravitational tidal tensor at the time of maximum expansion; this is the basis of the so-called tidal torque theory (hereafter TTT, Hoyle 1949; Peebles 1969; Doroshkevich 1970; White 1984; Catelan & Theuns 1996; Crittenden et al. 2001; Schäfer 2009, for a recent review). According to this theory, the spin direction should initially be correlated with

★E-mail: pichon@iap.fr

the principal axes of the local tidal tensor, defined as the traceless part of the Hessian matrix of the gravitational potential field. One therefore expects to detect correlations between actual galactic angular momenta and LSSs if non-linear processes have not modified their direction.

For many years, both observers and theorists have thus endeavoured to detect these correlations in real surveys and cosmological *N*-body simulations. None the less, the results remain in part contradictory because of the lack in resolution together with the difficulty of properly defining large-scale filamentary structures.

For instance, using *N*-body simulations Hahn et al. (2007a), Sousbie, Colombi & Pichon (2009) and Zhang et al. (2009) found that halo spins are preferentially oriented perpendicularly to the filaments whatever their mass, with Faltenbacher et al. (2002) measuring a random distribution of the spin in the plane perpendicular to the filaments, while Hatton & Ninin (2001) claimed an alignment between spin and filament. More recently a consensus seemed to have emerged when several works (Bailin & Steinmetz 2005; Aragón-Calvo et al. 2007; Hahn et al. 2007b; Paz, Stasyszyn & Padilla 2008) reported that LSSs – filaments and sheets – influenced the direction of the angular momenta of DM haloes in a way originally predicted by Sugerman, Summers & Kamionkowski (2000) and Lee & Pen (2000). These studies pointed towards the detection of a mass-dependent orientation of the spin, arguing for the first time that the spin of high-mass haloes tends to be perpendicular to their host filament, whereas low-mass haloes have a spin preferentially aligned with their host filament. Nevertheless, the detected correlation remains weak and noisy and no full explanation for these findings was highlighted except, for example, Bailin & Steinmetz (2005) who suggested that the spin direction of cluster and group mass haloes (as opposed to galaxy mass haloes) could come from mergers along the filaments.

However, Hahn, Teyssier & Carollo (2010) repeated this measurement in a cosmological hydrodynamical resimulation of one large-scale cosmic filament and found a different result: the spin of high-mass haloes is aligned with the filament; the spin of low-mass haloes is along the intermediate eigendirection of the tidal tensor in low-density regions and along the third eigendirection (i.e. neither the intermediate direction nor the filament's) in higher density regions at higher redshift ($z = 1$); finally, no signal exists for high-density regions at low redshift.

Beyond numerical simulations, Lee & Erdogdu (2007), Trujillo, Carretero & Patiri (2006), Navarro, Abadi & Steinmetz (2004), Flin & Godlowski (1990, 1986) and Godłowski & Flin (2010) found correlations in observations between the rotational axis of galaxies and the surrounding LSSs (e.g voids and local tidal shears) unlike Dekel (1985) who did not find any correlation. To be more specific, Flin & Godlowski (1986, 1990) first discovered that the spin of galaxies is not isotropically oriented with respect to the Local Supercluster plane but more likely to be aligned with it; Navarro et al. (2004) confirmed this observation; Trujillo et al. (2006) found that in SDSS and 2dFGRS, the rotational axis of the spiral galaxies located in the walls surrounding voids lie preferentially in the plane of these voids; Lee & Erdogdu (2007) analysed the galaxies of the 2MASS Redshift Survey and found correlations between their spin and the local tidal tensor and Godłowski & Flin (2010) focused on the galaxy groups in the Local Supercluster and found correlations in their orientation, suggesting that the two brightest galaxies and then the galaxy groups were hierarchically formed in the same filament with their major vector aligned with this host filament. The results of Navarro et al. (2004) and Trujillo et al. (2006) support the predictions of TTT (Lee & Pen 2000) namely that, assuming that the inertia and tidal tensors are uncorrelated, galaxies' spin should be preferentially aligned with the intermediate eigendirection of the tidal tensor (in particular in the plane of the voids). Recently, however, Slosar & White (2009) claimed that in contrast to previous studies, they found no departure from randomness in SDSS while studying the orientation of the galaxy spin with regard to the voids in which they are located. The method used in the latter study has been improved by Varela et al. (2012) who used the SDSS (DR7) and morphological classifications from the Galaxy Zoo project and found that galaxy discs are more likely to lie in the plane of voids, that is, their spin tends to be perpendicular to the void they are located in, which seems to be in disagreement with Lee & Erdogdu (2007), Trujillo et al. (2006) and Navarro et al. (2004).

In short, even if one can claim that a trend is slowly emerging, quantitative evidence of spin alignment with the filaments and tidal tensor eigendirections remains at this stage weak and somewhat inconclusive. Hence, in this paper, we propose to revisit the issue and quantify the alignment between the spin of DM haloes and the filamentary pattern in which they are embedded (together with the alignment between the spin and the tidal tensor principal axes) using a very efficient topological tool, the Skeleton (Sousbie et al. 2009). This tool provides a robust and mathematically well defined reconstruction of the cosmic web filaments. We apply it to the Horizon 4π simulation (Teyssier et al. 2009), a $2\,h^{-1}$ Gpc on a side cubic volume of the Universe containing over 67 billion DM particles which provides an unprecedented catalogue of 43 million DM haloes with masses $>2 \times 10^{11}\,\mathrm{M}_{\odot}$. We then interpret our results in the framework of the dynamics of large-scale cosmic flows.

Section 2 briefly presents the Horizon 4π simulation and the topological tool implemented to identify the loci and orientation of filaments. It then reports the correlations detected between the orientation of the spin of DM haloes and filaments and its redshift evolution. Section 3 is devoted to the physical processes that induce these correlations. It also illustrates them using DM halo merging histories, smoothed DM simulations and hydrodynamical simulations. Section 4 provides conclusions and discusses prospects for our understanding of galaxy formation within its cosmic environment. Appendix A gives the correlations measured between spin directions and tidal eigendirections, which are in agreement with the cosmic dynamics arguments of Section 2. Appendix B presents a visual quantitative estimation of the spin of the circumgalactic medium. Appendix C sums up all the tests we have performed to assess the robustness of the correlations presented in Section 2. Finally, Appendix D presents the dependence of the transition masses on the smoothing length and the non-linear mass as a function of redshift.

2 SPIN–FILAMENT CORRELATIONS

Let us first account for the robust correlation between the DM halo's spin and the orientation of the filaments of the cosmic web.

2.1 Virtual data sets

This study uses the Horizon 4π *N*-body simulation (Teyssier et al. 2009) which contains 4096^3 DM particles distributed in a $2\,h^{-1}$ Gpc periodic box to investigate the spin alignment of DM haloes relative to their LSS environment. This simulation is characterized by the following Λ cold dark matter (ΛCDM) cosmology: $\Omega_{\mathrm{m}} = 0.24$, $\Omega_{\Lambda} = 0.76$, $n = 0.958$, $H_0 = 73\ \mathrm{km\,s^{-1}\,Mpc^{-1}}$ and $\sigma_8 = 0.77$ within 1 standard deviation of *WMAP3* results (Spergel et al. 2003).

These initial conditions were evolved non-linearly down to redshift zero using the adaptive mesh refinement code RAMSES (Teyssier 2002), on a 4096^3 grid. The motion of the particles was followed with a multigrid Particle-Mesh Poisson solver using a Cloud-In-Cell interpolation algorithm to assign these particles to the grid (the refinement strategy of 40 particles as a threshold for refinement allowed us to reach a constant physical resolution of 10 kpc; refer to the above-mentioned two references).

The Friend-of-Friend (FoF) algorithm (Huchra & Geller 1982) was used over 18^3 overlapping subsets of the simulation with a linking length of 0.2 times the mean interparticular distance to define DM haloes. In this work, we only consider haloes with more than 40 particles, which corresponds to a minimum halo mass of $3 \times 10^{11}\,\mathrm{M}_\odot$ (the particle mass is $7.7 \times 10^9\,\mathrm{M}_\odot$). The mass dynamical range of this simulation spans about five decades. Overall, 43 million haloes were detected at redshift zero (see Fig. 1). This simulation was complemented by smaller (1024^3 particles, box size $200\,h^{-1}$ Mpc and several 256^3 particles, box size $50\,h^{-1}$ Mpc, leading to a particle mass of $6.2 \times 10^8\,\mathrm{M}_\odot$) DM-only simulations to address resolution issues (see Appendix C) and interpret the redshift evolution of the signal (see Section 2.3).

Several topological techniques (Barrow, Bhavsar & Sonoda 1985; Stoica et al. 2005; Novikov, Colombi & Doré 2006) have been proposed to identify the complex cosmic network made of large voids, sheet-like structures and elongated filaments. These techniques rely on giving a mathematical definition (and a detection algorithm) of the filamentary pattern that our eye easily detects in the simulations. One recent criterion to classify structures as clusters, filaments, sheets or voids uses the number of positive eigenvalues of the Hessian matrix of the density or potential fields (Aragón-Calvo et al. 2007; Hahn et al. 2007b; Forero-Romero et al. 2009). Another interesting approach was followed by Platen, van de Weygaert & Jones (2007, 2008) who used Watershed transforms to identify voids, filaments and walls. More recently, González & Padilla (2010) introduced a method which relies on positions and masses of DM haloes, and Bond, Strauss & Cen (2010) used Hessian eigendirections to detect filaments. In this paper, we use the (global) 3D Skeleton introduced by Sousbie et al. (2009). The underlying algorithm is based on Morse theory and defines the Skeleton as a set of critical lines joining the maxima of the density field through saddle points following the gradient. In practice, Sousbie et al. (2009) define the peak and void patches of the density field as a set of points converging to a specific local maximum/minimum while following the field lines in the direction/opposite direction of the gradient. The Skeleton is then a set of intersections of the void patches, that is, a subset of critical lines connecting the saddle points and the local maxima of a density field and parallel to the gradient of the field.

For this work, the ∼70 billion particles of the Horizon 4π simulation were sampled on a 2048^3 Cartesian grid and the density field was smoothed over 5σ using `mpsmooth` (Prunet et al. 2008), corresponding to a scale of $5\,h^{-1}$ Mpc and a mass of $1.9 \times 10^{14}\,\mathrm{M}_\odot$. Hence, we are focusing on the LSS of the cosmic web. The corresponding cube was then divided into 6^3 overlapping subcubes (with a buffer zone of 100 voxels in each direction, large enough to cover the largest peak patches of the simulation, see Sousbie et al. 2009), and the Skeleton was computed for each of these subcubes. It was then reconnected across the entire simulation volume to produce a catalogue of segments which locally define the direction of the Skeleton. This Skeleton is shown in Fig. 2. Note that this Skeleton (i.e. what we will call filaments in the rest of this paper) depends on the choice we made for the smoothing length ($5\,h^{-1}$ Mpc). Appendix D1 investigates the effect of probing smaller smoothing scales on other sets of simulations.

The hydrodynamical simulations used in this paper are described in Appendix B.

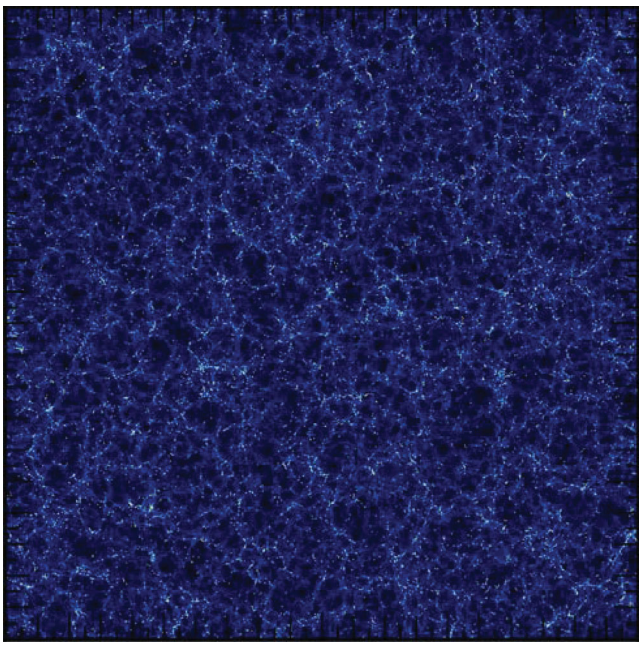

Figure 1. An 80 h^{-1} Mpc slice of the Horizon 4π simulation at redshift zero. The box size is $2\,h^{-1}$ Gpc across. On top of the DM log-density (colour coded in levels of blue, from dark to light), all haloes in that slice whose mass is larger than $3 \times 10^{13}\,\mathrm{M}_\odot$ are shown in the yellow dots. As expected, these haloes fall on top of the filamentary structure of the cosmic web.

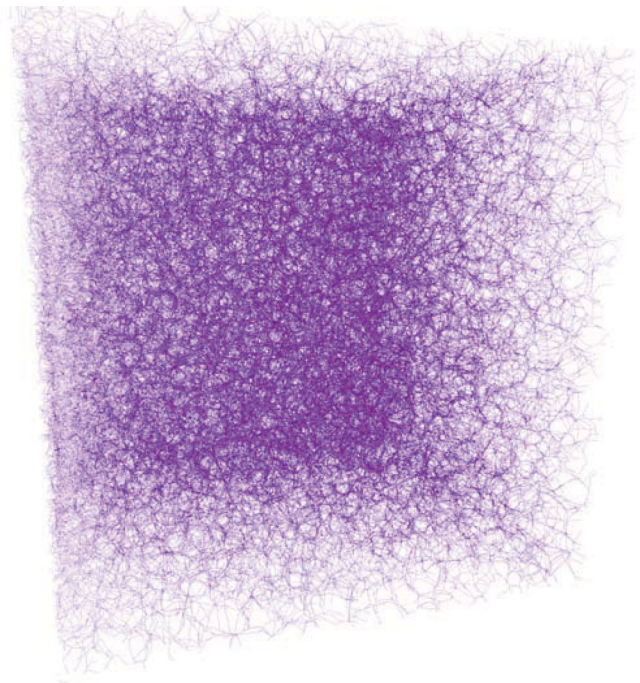

Figure 2. A 3D view of the Skeleton of the Horizon 4π simulation measured from the DM distribution. The size of the box is $2\,h^{-1}$ Gpc. This paper analyses the relative orientation of the spin of the 43 million dark haloes relative to the cosmic web.

2.2 Correlations between spin and filament axis

In order to study the alignment between the spin of haloes and the filamentary features of the cosmic web, we compute the Skeleton of the LSS for the density field smoothed with the above quoted Gaussian scale $R = 5\,h^{-1}$ Mpc which corresponds to $\sigma(R) = 0.66$. Thus, we are considering the filaments that are mildly non-linear LSSs at cluster scales.

In this paper, the spin of a given halo is defined as the sum over its particles denoted by i: $m_{\rm p}\sum_i(\boldsymbol{r}_i - \bar{\boldsymbol{r}}) \times (\boldsymbol{v}_i - \bar{\boldsymbol{v}})$, where $\bar{\boldsymbol{r}}$ is the centre of mass of the FoF halo and $\bar{\boldsymbol{v}}$ is its mean velocity. We search for the five DM haloes (regardless of their mass) closest to *each* filament segment (see Appendix C for alternative choices). We then measure the angle between the angular momentum of these haloes and the direction of the filament segment and estimate the probability distribution function (PDF) of the absolute value of the cosine of this angle; this PDF, $1 + \xi$, measures the excess probability of alignment between the halo spin and the direction of the filament (note in particular that it is normalized for $\cos\theta$ between 0 and 1; for aesthetic purpose only, data are symmetrically plotted for $\cos\theta$ between -1 and 1; Appendix C briefly discusses the associated biases). The data are split by halo masses ranging from galactic to cluster masses and are displayed in Fig. 3, the main result of this paper.

A clear signal is detected. The orientation of the halo spin depends on the local anisotropy of the cosmic web, *and* on the DM halo mass: the spin of DM haloes is preferably perpendicular to their host filament at high mass (with an excess probability reaching 12 per cent), but turns into being aligned with the nearest filament direction at lower masses (with an excess probability of 15 per cent). This 'phase transition' is found to occur at $M^{\rm s}_{\rm crit}(z = 0) \simeq 4(\pm1) \times 10^{12}\,{\rm M}_\odot$, where $M^{\rm s}_{\rm crit}$ is defined as the halo mass for which $\langle\cos\theta\rangle = 0.5$. Fig. 4 shows an example segment of the large-scale filamentary network together with the orientation of spins of massive haloes that graphically demonstrates for them the effect of spin–filament anti-alignment. Several sanity checks have been carried out to assess the robustness of this signal and are summed up in Appendix C.

These measurements of the spin–filament correlation trend confirm the previous results obtained by Bailin & Steinmetz (2005), Aragón-Calvo et al. (2007), Hahn et al. (2007b) and Paz et al. (2008) with significantly improved statistics which allow us to quantify the mass transition.

2.3 Redshift dependence of the transition mass

The redshift dependence of the transition mass was then investigated on a set of smaller ΛCDM simulations (1024^3 particles in $200\,h^{-1}$ Mpc periodic boxes and 256^3 particles in $50\,h^{-1}$ Mpc periodic boxes). At high redshift we define the filamentary structure at the smoothing scale, $R(z)$, chosen to maintain the same level of non-linearity as we had at redshift zero for $R_0 = 5\,h^{-1}$ Mpc. Thus, the smoothing scale $R(z)$ is obtained from the implicit condition $\sigma^2(R(z), z) = \sigma^2(R_0, 0)$ (see Appendix D2). The halo spins continue to exhibit a transition from alignment with the nearest filament at low mass to anti-alignment at high mass. The critical mass for the transition, $M^{\rm s}_{\rm crit}(z)$, is found to decrease with redshift as a power law

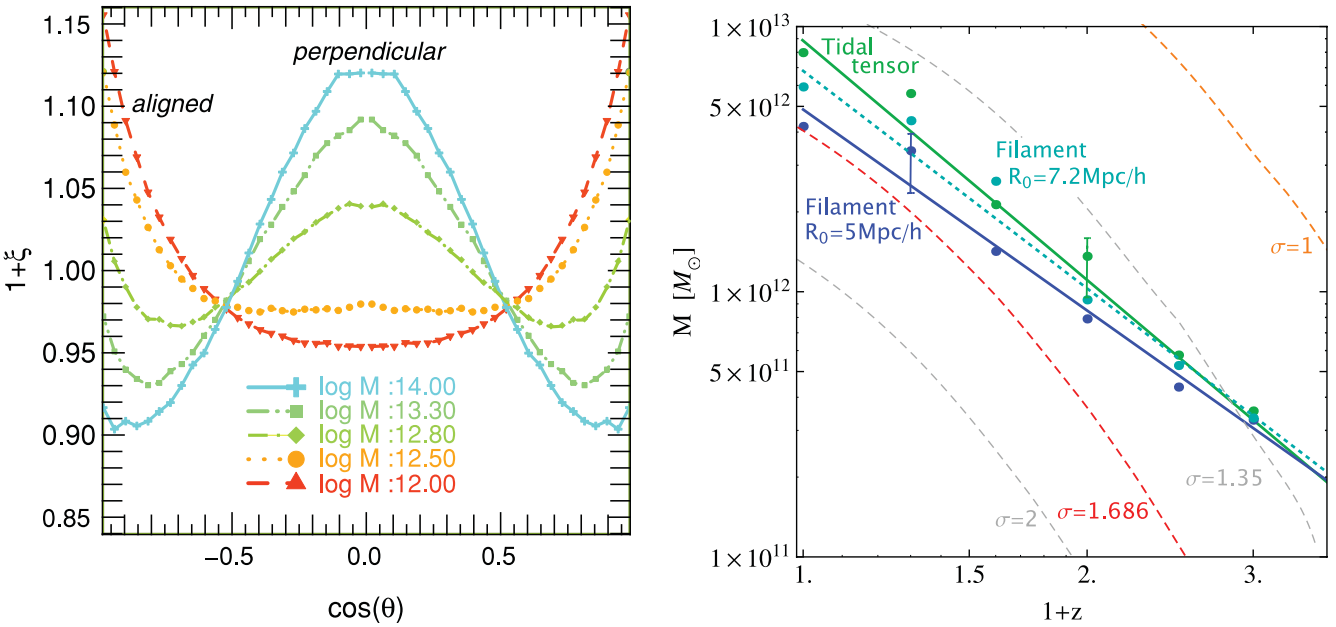

Figure 3. Left-hand panel: excess probability of alignment between the spin and the direction of the closest filament as measured from the 43 millions haloes of the Horizon 4π simulation at redshift zero. Different colours correspond to different mass bins from 10^{12}(red) to $10^{14}\,{\rm M}_\odot$ (blue) as labelled. Thanks to the very large number of haloes in each mass bin, the excess probability is quite well sampled and displays a clear departure from a uniform distribution. A transition mass is detected at $M^{\rm s}_0 = M^{\rm s}_{\rm crit}(z = 0) \simeq 5(\pm1) \times 10^{12}\,{\rm M}_\odot$: for haloes with $M > M^{\rm s}_0$, the spin is more likely to be perpendicular to their host filament, whereas for haloes with $M < M^{\rm s}_0$, the spin tends to be aligned with the closest filament. Right-hand panel: redshift evolution of the filament transition mass (in blue) and the tidal tensor transition mass (in green) derived from the $200\,h^{-1}$ Mpc ΛCDM simulations as discussed in the main text. The (cyan) dotted line represents the spin–filament mass transition for a larger smoothing length ($7.2\,h^{-1}$ Mpc). The displayed error bar is estimated as one-third of the bin mass. The dashed lines correspond to the non-linear masses (for a top-hat filter, see Appendix D2) at different σ, in particular $\sigma = 1$ (orange) and $\sigma = 1.686$ (red). The redshift evolution of the transition masses is in qualitative agreement with that of $M_{\rm NL}(\sigma \lesssim 1.686)$ though they seem to remain close to power laws throughout the explored range of redshift.

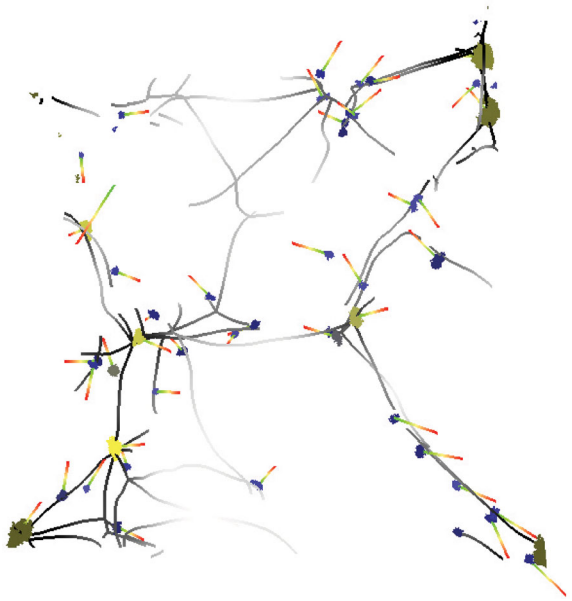

Figure 4. A very small subset of Skeletons at different redshifts extracted from the Horizon 4π simulation (see Fig. 2), together with unit vectors showing the orientation of the spin of the corresponding DM halo with a mass above the transition mass. The spin is indeed perpendicular to the filament for these massive haloes.

of z. Namely,

$$M^{\rm s}_{\rm crit} \approx M^{\rm s}_0(1+z)^{-\gamma_{\rm s}}, \quad \gamma_{\rm s} = 2.5 \pm 0.2, \quad M^{\rm s}_0 \simeq 5\times10^{12}\,{\rm M}_\odot. \tag{1}$$

This result is presented in Fig. 3 over the studied range $z = 0$–4. Measuring the dependence of the $z = 0$ transition mass M_0 on scale R_0 (see Fig. D1), we find some weak scaling, $M^{\rm s}_0 \propto R_0^{0.8}$. Note that this dependence significantly depends on redshift.

The existence and redshift dependence of the transition mass in spin–structure alignment is supported by studying the halo's spin direction relative to the orientation of the large-scale gravitational tidal tensor. The details are given in Appendix A, where we find that the more massive haloes are preferably aligned with the intermediate principal axis of the tidal tensor, while smaller haloes show a positive alignment with the minor axis (which near a filament is the direction in which the filament extends). In this approach, our measurements give for the transition mass

$$M^{\rm t}_{\rm crit} \approx M^{\rm t}_0(1+z)^{-\gamma_{\rm t}}, \quad \gamma_{\rm t} = 3 \pm 0.3, \quad M^{\rm t}_0 \simeq 8\times10^{12}\,{\rm M}_\odot, \tag{2}$$

in good agreement with the Skeleton results, equation (1). The somewhat larger amplitude of $M^{\rm t}_0$ with respect to $M^{\rm s}_0$ can be explained by noticing that the tidal tensor associated with the gravitational potential smoothed on a scale R_0 effectively probes larger scales than the smoothed density field itself. Fig. 3 shows that if we boost the smoothing scale used to define the Skeleton to $R_0 = 7.2\,h^{-1}$ Mpc, $M^{\rm s}_{\rm crit}$ and $M^{\rm t}_{\rm crit}$ will match very closely (see also Appendix D1).

In Fig. 3, we also compare $M_{\rm crit}(z)$ to the redshift evolution of the mass scale $M_{\rm NL}(z)$ that corresponds to the fixed $\sigma(R, z)$ (defined in Appendix D2). Several values of the variance are of interest to track. One is $\sigma(R, z) = 1$ which formally defines the scale of non-linearity. Another is $\sigma(R, z) = 1.686$ which corresponds to the characteristic mass scale, $M_\star$, of collapsed gravitationally bound haloes at redshift z in the spherical top-hat model. Even though it is clear from Fig. 3 that both transition masses $M^{\rm s}_{\rm crit}$ and $M^{\rm t}_{\rm crit}$ qualitatively match a non-linear mass evolution with $\sigma \lesssim 1.686$ at low redshifts, at high z they still follow a power-law behaviour, while $M_{\rm NL}$ steepens as it probes the steepening power spectrum at ever shorter scales. Thus, at high redshifts, the positive alignment between the halo's spins and the nearby filaments extends to masses that are effectively higher, in terms of the corresponding characteristic non-linear mass. Although we do not have the full quantitative explanation for this effect, it may be related to the fact that the filaments at high z are more pronounced due to a steeper power spectrum, and are correlated with the shear of the surrounding flow more robustly. Note that the detection of haloes and filaments at these redshifts may be a concern for these intermediate-resolution simulations. Whilst we defer a detailed quantitative understanding of the redshift evolution of the mass transition, the rest of this paper is devoted to *explaining* the origin of these mass transitions.

3 SPIN INDUCED BY LSS DYNAMICS

The measurements of Section 2.2 strongly suggest that the spin direction of DM haloes is connected to the cosmic web. Indeed, these dark haloes are embedded in large-scale cosmic flows induced by the successive formation of walls, filaments and clusters: matter escapes from the voids to the walls then to the filaments before flowing along the latter direction towards the nodes (Zel'Dovich 1970; Bond et al. 1996; Pichon et al. 2011). In this framework, let us now argue that the first generation of haloes are formed during the *winding of walls around filaments*, which provides them with a spin parallel to this direction (and whose amplitude is proportional to the relative impact parameter of the two walls). Conversely, the later generations of haloes form by mergers along the filaments, that is, in the direction parallel to the mean flow (as was first pointed out by Sousbie et al. 2008) and therefore acquire a spin perpendicular to the filaments (if the orbital angular momentum which is converted into spin during the merger dominates). In this scenario, the transition in mass measured in Fig. 3 in fact reflects a trend in merging generation.[1] Note that this behaviour occurs on several scales simultaneously; this multiscale signal is probed by varying the smoothing scale used to define the filaments in Appendix D1.

As a first check for this hypothesis, the typical distance of DM haloes from filaments is computed as a function of their mass. The more massive haloes are typically found closer to the filaments (on average at 0.7 h^{-1} Mpc) than low-mass haloes (found on average at 2 h^{-1} Mpc from the core of the filaments), which is consistent with our assumption because it implies that high-mass haloes have reached the centre of the filaments, where they are more likely to merge in the direction of the flow. Conversely, low-mass haloes (for which large-scale dynamics have been frozen in at an early stage) are found farther from the core of the filaments where they are less likely to merge. This is qualitatively consistent with Fig. 1, which shows the distribution of massive haloes within a slice of the simulation.

3.1 Winding up of DM flows

Let us have a look at Fig. 5, which displays the temporal evolution of DM particle trajectories in the vicinity of a DM filament. This simulation has the special feature that the small-scale modes were

[1] Technically, it was not possible to build merging trees a posteriori on the Horizon 4π simulation as it would have required too many snapshots and thus too much disc space; so we did carry out the tests described in Section 3.2 on a smaller simulation to confirm the relevance of merger generation as the key parameter.

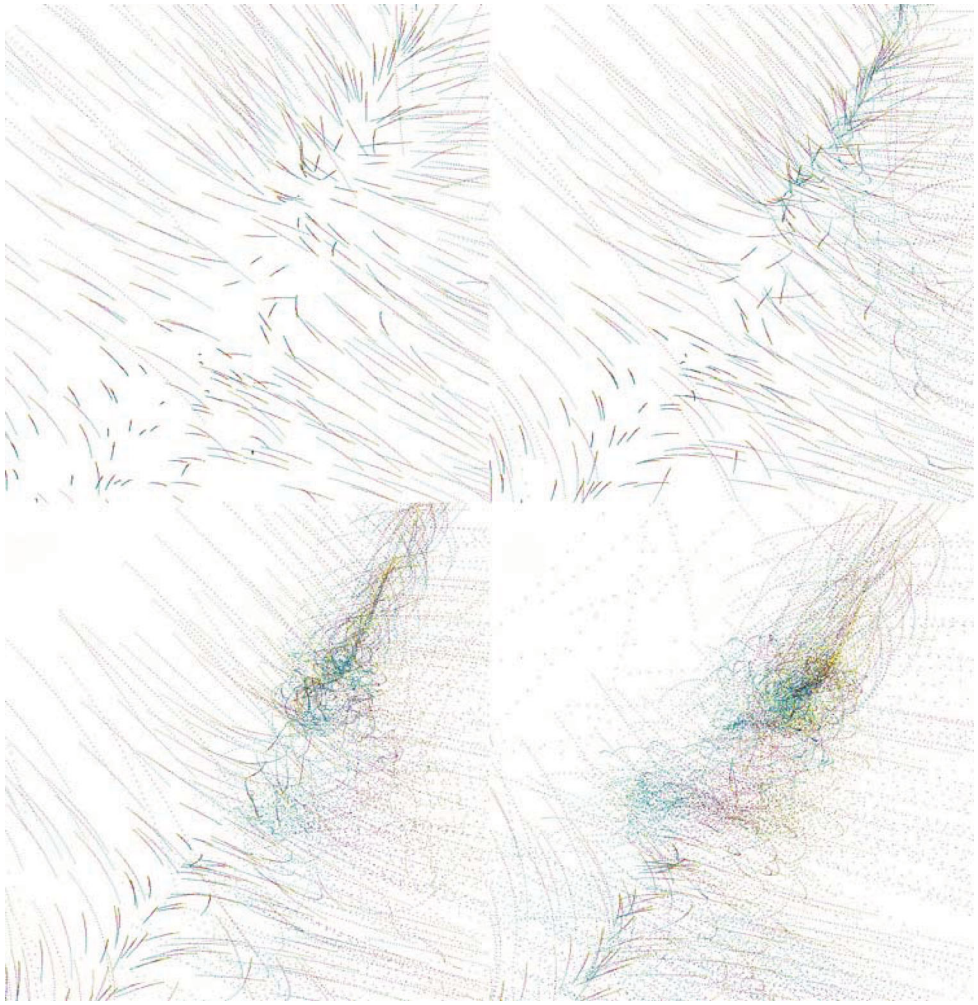

Figure 5. Trajectory of DM particles, colour coded from yellow (early) to blue (late) via dark red as a function of time. The four panels (from the top to bottom and left-hand to right-hand side) correspond to different stages of the winding of two walls around a north-eastern-oriented filament. Once DM has joined the filament, it heads towards the bottom left-hand part of the panel in the direction of a more massive node of the cosmic network. This process is best seen dynamically at http://www.iap.fr/users/pichon/spin/.

erased from the initial conditions in order to facilitate visualization of the large-scale flow (see Pichon et al. 2011 for details). We refer to this simulation as a 'smoothed' simulation. Here most of the flow is in fact embedded in a large wall parallel to the plane of the figure. The dots with different colours (from yellow to blue via dark red) correspond to the position of the same DM particle at successive time-steps, and thus allow us to visually follow the trajectory of DM particles. The top left-hand panel corresponds to a snapshot somewhat before the flow has significantly shell crossed around the north-eastern filament. The DM particles are plunging towards their filament, while flowing within the two walls. In the top right-hand panel, some level of shell crossing has occurred in the north-eastern part of the filament, and the corresponding particles have started inflecting their trajectories to wind up around the locus of that filament. Since these particles typically have a non-zero impact parameter relative to the centre of mass, as they wind up, they convert their orbital motion into spin while generating a virialized structure. Later on (bottom left-hand panel) this structure sinks along the north-eastern filament towards a more massive clump (off field). Meanwhile, the process of DM winding from the walls around the main filament continues, and feeds (as a yellow trail) the DM halo along its current spin axis (which is aligned with the axis of the filament). Finally, in the bottom right-hand panel, another such halo has formed farther down the filaments, and we can anticipate that their upcoming merger will lead to a structure whose spin's direction will be a mixture of their initial spin and the spin perpendicular to their relative orbital plane. In Section 3.3 below, we will revisit this scenario using hydrodynamical simulations, which will allow us to visually identify the spin of forming galaxies.

3.2 The progenitors of dark haloes via merging trees

In order to understand the previously described mass transition and its redshift evolution, we used the code TreeMaker (Tweed et al. 2009) to track down the progenitors (both dark haloes and unresolved flows) of given haloes in conjunction with their spin orientation relative to the nearest filament. TreeMaker involves two steps: first, haloes are identified using a halo finder – in our case a FoF algorithm (Huchra & Geller 1982; Zeldovich, Einasto & Shandarin 1982; Davis et al. 1985), while the properties of these structures (mass, angular momentum, etc.) are measured. As the second step, the individual DM particles which belong to each halo are tracked back in time so as to build a merging history tree which regroups all of its progenitors and their properties as a function of

time. A relatively large number of merging trees were computed and the direction of the spin of the progenitors relative to their host filament was calculated.

After visual inspection of a subset of those merging trees, it was found that: (i) the high-mass haloes (i.e. above the critical mass) with a spin perpendicular to their filament tend to have a similar history: they often acquire a significant amount of mass via a major merger, which is accompanied by a significant spin adjustment from a direction initially aligned with their filament to a direction mostly perpendicular to their filament (and aligned with $\boldsymbol{e}_2$, see Appendix A); and (ii) in contrast, low-mass haloes (i.e. below the critical mass) are not the result of major mergers; often no mergers at all are found at the mass resolution of the N-body simulations; those who have a spin parallel to the filament seem to have acquired this spin direction at a time (the so-called formation time) when they have acquired most of their mass by diffuse accretion.

This behaviour is quite generic as we observed it for a few tens of randomly chosen haloes. It is illustrated in Fig. 6 where merging trees of two different haloes (extracted from one of the 50 h^{-1} Mpc ΛCDM simulations) are shown: the evolution of the angle between the closest filament and the spin of a given halo is plotted as a function of redshift; the colours encode the fraction of mass of the progenitor with respect to the final halo mass. The right-hand panel corresponds to a low-mass halo ($2 \times 10^{11}\,\mathrm{M}_\odot$ at redshift zero corresponding to more than 300 particles) which forms at redshift $z \simeq 1.5$ (when it has already acquired more than one half of its mass) and suddenly acquires a spin parallel to its closest filament at a high redshift ($\simeq$2) close to its formation time. This halo does not undergo any significant merger afterwards. Conversely, the left-hand panel provides the merging tree of a high-mass halo ($8 \times 10^{12}\,\mathrm{M}_\odot$ at redshift zero) which forms at lower redshift ($\simeq$0.4) as the result of a major merger between two less massive haloes. This event corresponds exactly to the time when it acquires a spin perpendicular to its closest filament. What is striking here is the clear flip of the spin direction: the two progenitors have a spin aligned with the filament (this spin is acquired at higher redshift $\simeq$1.5) and their merger makes the spin of the resulting halo become perpendicular to it. These two examples of trees are characteristic of how haloes below and above the critical mass $M^{\mathrm{s}}_{\mathrm{crit}}$ form and acquire spin. Note that we actually observe a large dispersion of the histories around this mean behaviour.

To check the statistical robustness of this scenario for low-mass objects, let us identify a preferred plane of motion at formation time. The following simple test was implemented: a set of low-mass haloes ending with a spin parallel to their closest filament are randomly chosen and only haloes for which a time of significant accretion (i.e. their formation time) can be determined are retained (this represents at least one-third of our sample). Their particles are traced back one time-step before their formation time to quantify the relative orientation of their velocities compared to the filament's direction. The excess probability distribution of alignment, $1 + \xi_V$, is shown in Fig. 7 and shows that their velocities (before formation) are more likely to lie perpendicular to the filament (in particular it is found that $\langle \cos\theta_V \rangle \simeq 0.47$), which is in agreement with the scenario (see also Fig. A1).

In order to assess the statistical relevance of the scenario for massive haloes (i.e. above the critical mass at redshift zero), merging trees can also be used to determine their most recent merger. The mean cosine of the angle between these haloes and their host filament just after merging is computed and compared to the mean cosine of the angle between the closest filaments and the spin of the progenitors just before merging. This test yields $\langle \cos\theta \rangle \simeq 0.51$ before and 0.47 after the last merger, which is fully consistent in amplitude with the mean cosines found for the Horizon 4π simulation [for which, for instance, $\langle \cos\theta \rangle \simeq 0.510$ (0.479) for $M \simeq 10^{12}\,\mathrm{M}_\odot$ ($M \simeq 10^{13}\,\mathrm{M}_\odot$)]. The 1$\sigma$ error on the mean is about $\pm$0.02, given the size of this sample (only $\simeq$ 200 haloes massive enough in this simulation). This statistical test is in agreement with the fact that massive haloes acquire a spin perpendicular to their host filament because of mergers.

Altogether, we are now able to reconstruct the history of spin acquisition by DM haloes following the large-scale dynamics. The

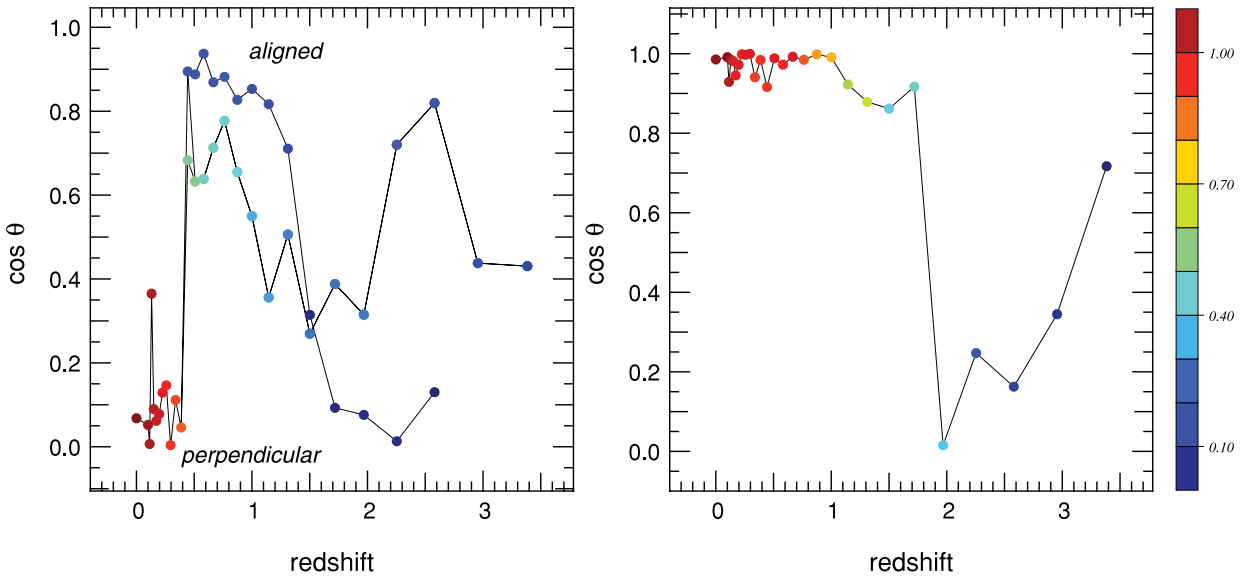

Figure 6. Left-hand panel: merging tree of a high-mass halo ($8 \times 10^{12}\,\mathrm{M}_\odot$ at redshift zero). The various colours correspond to different mass fractions (relative to $z = 0$). The vertical axis corresponds to the angle between the host filament and the spin of this halo, and the horizontal axis to the redshift. Here, the spin becomes perpendicular to its filament after an important merger at redshift ~ 0.5. Right-hand panel: merging tree of a low-mass halo ($2 \times 10^{11}\,\mathrm{M}_\odot$ at redshift zero). Here, the spin becomes suddenly parallel to its host filament when the halo acquires most of its mass by accretion between redshift 1 and 2.

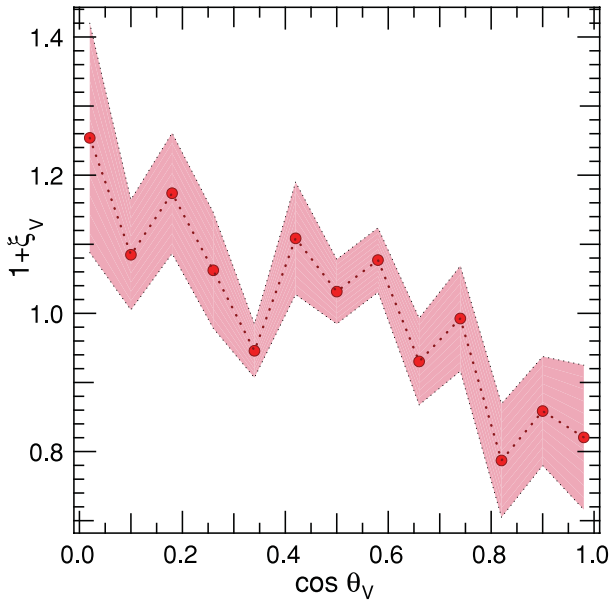

Figure 7. Excess probability of the velocity–filament alignment just before the formation time for a sample of 15 low-mass haloes ($M < M_{\rm crit}$). The average orientation over these 15 haloes is plotted with a dotted line, while the 1σ deviation away from that mean is displayed in pink. The progenitors' velocities before formation lie preferentially in a plane perpendicular to the closest filament (see also Figs 6 and A1).

less massive objects are born by accretion at high redshift during the winding of the walls into filaments. This process generates a spin aligned with the filaments. Most of the haloes of low mass at $z = 0$ are now formed, and their spin will not change much because they have already acquired most of their mass while future accretion will not be important enough to have a strong impact on their spin direction. This behaviour is illustrated in Fig. 6 (right-hand panel) where a halo forms and acquires a spin parallel to the direction of the forming filament, which then remains in the same direction during accretion until redshift zero.

At lower redshift, filaments are collapsing and thus create a flow along their direction in which the more massive haloes form by major mergers. During this process, these massive haloes acquire a spin which is the superposition of the spin of their progenitors and the orbital spin from the merger. As the motion is along the filament, this orbital spin is in a plane perpendicular to it. This process is shown in Fig. 6 (left-hand panel): the spin of the (less massive) progenitors is parallel to the filaments and their merger within the filaments induces a more massive halo whose spin is now perpendicular to the host filament. For these more massive DM haloes, a competition between orbital spin and intrinsic spin during the merger process has just been highlighted and explains the resulting orientation. Indeed, their spin is not randomly distributed in a plane perpendicular to the filaments but is shown to be correlated with one particular eigendirection of the large-scale tidal tensor. This issue is fully addressed in Appendix A.

It is interesting to compare the picture described above with Peirani, Mohayaee & de Freitas Pacheco (2004) who focused on the spin magnitude (instead of its direction). These authors claimed that spin acquisition was dominated by merger events, rather smooth accretion; Fig. 6 suggests that this holds true for the spin's direction of haloes more massive than the critical mass $M^{\rm s}_{\rm crit}$ as well.

3.3 Visual inspection using hydrodynamics

For illustrative purposes, let us now turn to a high-redshift hydrodynamical simulation, as the cold gas that we will analyse here follows more closely the caustics of the cosmic web than the DM, and thus provides a clearer visual impression of the process of wall winding and spin acquisition (in contrast to collisionless DM, cold gas does not undergo shell crossing but shocks and loses degrees of freedom – its motion perpendicular to the shock). We are not concerned here with how much respective angular momentum gas has with respect to DM acquired, but only use hydrodynamics as a proxy for pinpointing more accurately the loci of shell crossing and identifying the spin axis of galaxies. As we will argue later, it is also of interest to consider in parallel the environment of low-mass, high-redshift and high-mass, low-redshift haloes. Following Dubois et al. (2012) we use tracer particles of the gas in a cosmological hydrodynamical simulation (which is described in Appendix B) to illustrate this winding of walls and the loci and orientations of galaxies.

Fig. 8 represents the web-like filamentary structure of the gas at $z = 9$ in a field of size approximately $50\,h^{-1}$ kpc across; the ensemble of tracer particles initially makes up a sheet-like structure with a dominant filament embedded in it. Note that these tracer particles represent a biased subset of all tracers as they are chosen so as to end up within the bulge of the main galaxy of this zoom-in simulation at some later stage. The tracer particles flow from this sheet into the filaments where they form 'protogalaxies'. The gas thereby typically has a non-zero impact parameter relative to the filament and protogalaxies thus acquire a spin parallel to the filament in which they form (see the arrows in the figure). These young galaxies then migrate along their filaments and merge with other galaxies. The spin of the merger remnant is a combination of the orbital angular momentum of the collision and the initial spin of the progenitors; it can therefore depart from the direction of the host filament. We provide an animation at http://www.iap.fr/users/pichon/spin/ which allows this to be seen more easily (see also the Supporting Information with the online version of the paper). Fig. B1 illustrates quantitatively the visual impression of Fig. 8 while measuring the spin of the circumgalactic discs (between 0.1 and $0.25R_{\rm vir}$).

In Fig. 9, a small subset of these tracer particles are randomly chosen and followed for a while from early (left-hand panel) to late times (right-hand panel). On large scales (at early times), we note that the flow is indeed dominated by the winding up of matter from the main wall around the main filament. The tracers' trajectories start perpendicular to the filament within the walls. As they reach the filament, they take a sharp turn, losing their transverse motion and flowing along the filament (left-hand panel). In doing so, since the laminar flows on opposite sides of the wall will typically have different impact parameters, they generate a spinning structure whose axis will be aligned with the filament. This spaghetti structure converges into a quite narrow and elongated plait on either side of the forming disc. Given its orientation, the induced disc will therefore advect secondary infall at its periphery preferentially along its spin axis (as both the galaxy and its upcoming secondary infall were assembled via the same winding process).

In a nutshell, the cold gas dynamics of large-scale cosmic flows provide a much clearer illustration of the scenario we outlined for the formation of haloes with a spin mostly aligned with the local filament. We do not discuss any further the properties of the alignment of the disc with respect to the filamentary structure, given that there exist many caveats (though see Section 4.2 below and Appendix B).

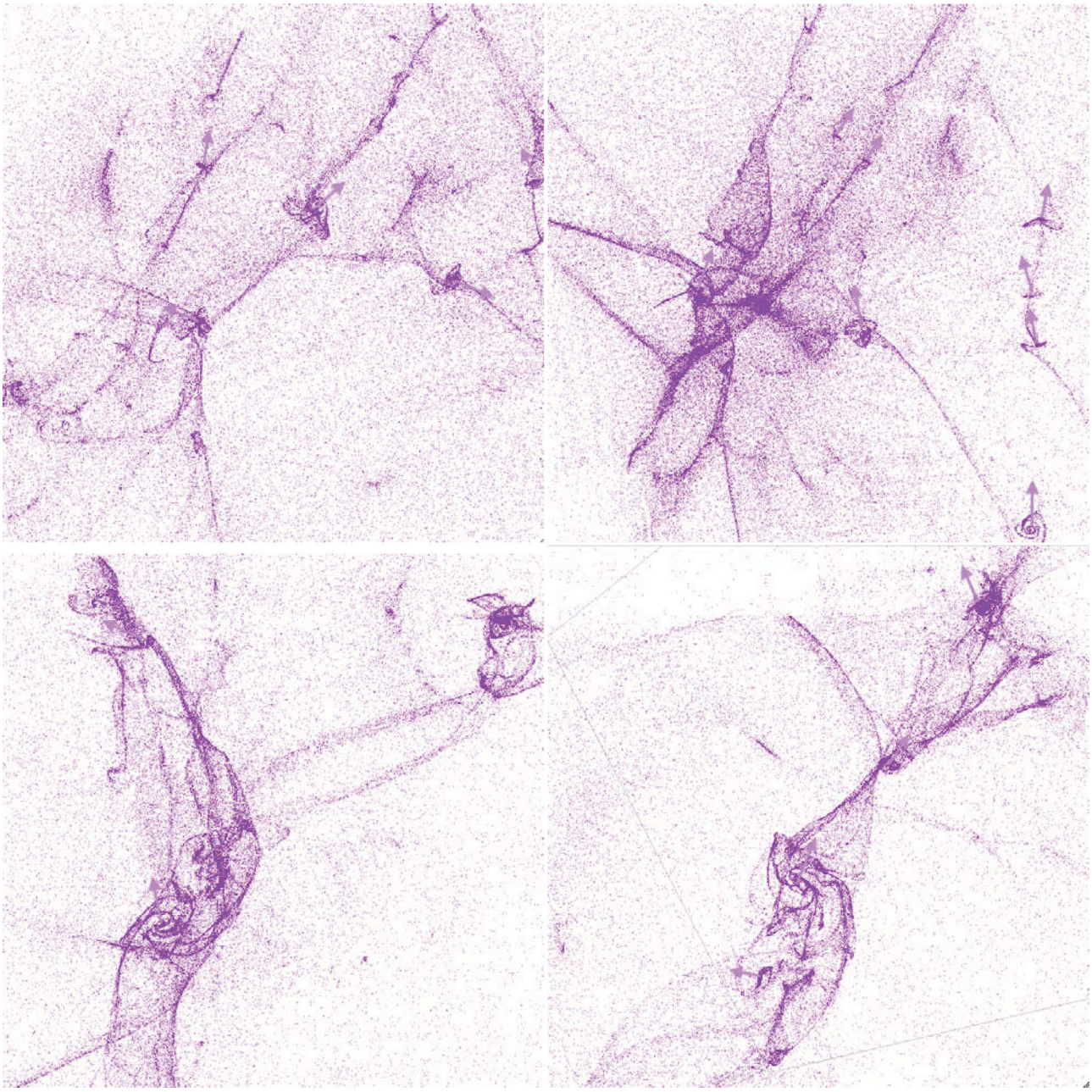

Figure 8. Distribution of hydrodynamical tracer particles (at $z \simeq 9$, top panels, and $z \simeq 8$, bottom panels). The web-like filamentary structure (top left-hand and right-hand panels) of the gas distribution which ends up in the bulge of a unique galaxy at later times is quite intricate, though one main wall in which the largest filament is embedded dominates (seen more clearly edge-on, in the top right-hand panel). Note the disc-like features with a spin parallel to the filament (represented qualitatively as an arrow perpendicular to the disc). Bottom panels: zoom-in at a later stage to visualize the process of a merger along the filament, before (bottom left-hand panel) and during (bottom right-hand panel) the merger. The spin of the merger remnant is a combination of the orbital angular momentum and the initial spin of the progenitors; it can therefore depart from the direction of the host filament. Note also the ribbon structure of filaments which corresponds to the locus of the second shock. Visual inspection suggests these ribbons become broader with time (as predicted by Pichon et al. 2011 as they advect larger and larger amount of angular momenta from the outskirts of the gravitational patch) and tend to lie perpendicular to the main wall; as they reach the protogalaxy, they twist rapidly on outer shells and build up its outskirts.

4 CONCLUSIONS AND PROSPECTS

In this paper, the Horizon 4π N-body simulation was used to investigate the correlations between the spin of DM haloes and their large-scale environment. For filaments defined over a smoothing scale of $5\,h^{-1}$ Mpc, a statistically significant signal was detected, indicating that the orientation of the spin of DM haloes is sensitive to the cosmic environment. A mass dependence of this signal was also robustly established: low-mass haloes are more likely to be aligned with large-scale filaments (with an excess probability of 15 per cent), whereas more massive haloes tend to be perpendicular to these (with an excess probability of 12 per cent). The mass transition was found to be redshift-dependent and to vary like $M_{\rm crit}(z) \approx M_0(1+z)^{-\gamma}$ with $M_0^{\rm s} \simeq 5(\pm1) \times 10^{12}\,{\rm M}_\odot$ and $\gamma_{\rm s} = 2.5 \pm 0.2$. This critical mass is also found to increase with smoothing length (Appendix D1). These results are in agreement with those presented

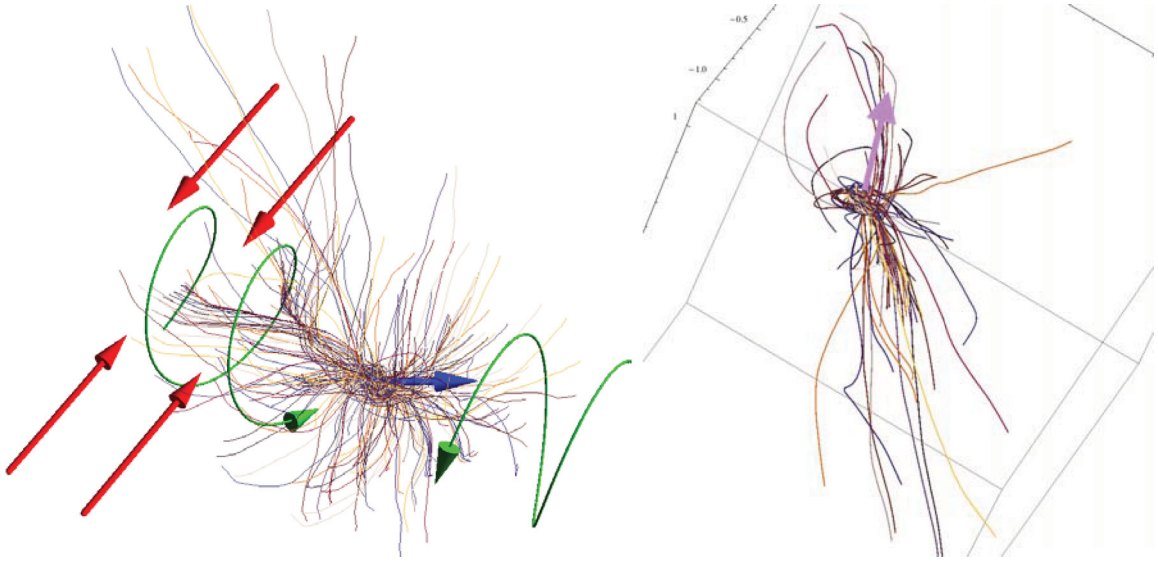

Figure 9. Trajectories of tracer particles in the outer region (left-hand panel) and inner region (right-hand panel). On large scales, the gas departs from voids, flows along the walls (red arrows) and winds up in filaments along well-defined ribbons (green arrows), forming low-mass haloes. In the inner region of the tracks, the flow is indeed along the filament and spiralling in into a disc whose axis is roughly aligned with the filament.

in Appendix A, which are derived using a more classic approach of considering excess alignment of the halo spin with the tidal tensor eigendirections. Since the tidal tensor probes larger scales than the Skeleton of the density, the mass transition is detected for a larger mass $M_0^{\rm t} \simeq 8(\pm 2) \times 10^{12}\,{\rm M}_\odot$, which scales slightly differently with redshift, that is, $\gamma_{\rm t} = 3 \pm 0.3$. Both redshift evolutions are roughly consistent with that of the formal non-linear mass scale.

4.1 Discussion

This unambiguous result confirms and quantifies recent findings (Bailin & Steinmetz 2005; Aragón-Calvo et al. 2007; Hahn et al. 2007b; Paz et al. 2008). It is also consistent with Sousbie et al. (2009) who found that the spin of DM haloes tends to be perpendicular to filaments. Indeed, weighting our statistics by the spin magnitude (which corresponds to their strategy), we recover their results. Zhang et al. (2009) found the same result, but did not have enough statistics to probe the signal above the critical mass. The study of Faltenbacher et al. (2002) focused on haloes above $10^{14}\,h^{-1}\,{\rm M}_\odot$, that is, above the critical mass at redshift zero, which is why, in agreement with this work, they found a trend for these haloes to have a spin perpendicular to their closest filament. In contrast, Hatton & Ninin (2001) considered haloes with mass around 10^{11}–$10^{12}\,{\rm M}_\odot$, that is, below the critical mass and thus found an alignment of the spins with the filaments, again in agreement with this work. This paper also confirms the very recent findings of Libeskind et al. (2012) who claimed that low-mass haloes (around 10^{10}–$10^{11}\,{\rm M}_\odot$) tend to be aligned with the filaments and to lie in the plane of walls.

Note that Appendix A predicts a strong trend for the spin vector of DM haloes to lie in the plane of large-scale walls. Such a signal was claimed to have been detected in observations by Lee & Erdogdu (2007), Trujillo et al. (2006), Navarro et al. (2004) and should be re-investigated in view of this paper's predictions. Furthermore, observers should now also be able to investigate the spin–filament correlations in a way directly comparable to the theoretical predictions for DM presented in this paper (Fig. 3). Indeed, the code DisPerSE (Sousbie 2011), which identifies filaments using persistence, can accurately deal with discrete and sparse data sets and should provide a good estimator for the direction of *observed* filaments.

The time evolution of the angular momentum of individual DM haloes obtained by following their progenitors using merger trees suggests that the spin direction results, on the one hand, from the winding of the walls into filaments (first-generation, low-mass haloes) and, on the other hand, from significant mergers occurring along those filaments (second-generation, more massive haloes). More specifically, the arguments we developed throughout this paper strongly suggest that the measured correlations can be understood as a consequence of the dynamics of large-scale cosmic flows. Indeed, low-mass haloes mostly form at high redshift within the filaments generated by colliding/collapsing walls. Such a process naturally produces a net halo spin parallel to the filaments. In contrast, high-mass haloes mainly form by merging with other haloes along the filaments at a later time when the filaments are themselves colliding/collapsing. Therefore, they acquire a spin which is preferentially perpendicular to these filaments. Visual examination of 'smoothed' DM and hydrodynamical simulations lends extra support to this picture (see also Appendix B). Measurements of the orientation of the spin relative to the eigenvectors of the tidal tensor are also consistent with such a scenario, provided one takes into account the fact that they probe typically larger scales of the density field.

From the point of view of a large-scale filament, most low-mass haloes are formed early from patches that are part of a planar, flattened inflow of matter on to that filament. For Gaussian random fields, the tidal tensor in such patches is correlated with the filament's direction (via the shape parameter γ, Pogosyan et al. 2009), resulting in the preferential alignment of the spin of such haloes along that filament. This process is related to the theoretical predictions of Pichon & Bernardeau (1999) who demonstrated, using the Zel'dovich approximation, how vorticity was generated during the first shell crossing. This vorticity will lie in the plane of the forming walls. Extending their predictions while focusing now on a 2D flow, we speculate that secondary shell crossing will lead to the formation

of vortices aligned with the forming filament (see figs 5 and 7 of Pichon & Bernardeau 1999, a possible section perpendicular to the axis of the filament).[2] In turn, these vortices could account for the spin of protogalaxies, as was suggested by the referee of that paper.

The excess probability in Figs 3 and A2 lies at the 15–40 per cent level. As such it mainly reflects a residual trend of coherence inherited from the large-scale cosmic environment in which haloes form. This does not preclude the multiscale hierarchical clustering process from erasing part of this more orderly dynamics. For instance, clustering and merging on smaller scales will in part perturb large-scale ordered ribbons (as is already visible in the bottom panels of Fig. 8).

The trend in Fig. 3 is found, on the one hand, in these measurements at the high end of the mass function at redshift zero (whose dynamics is only mildly non-linear) and, on the other hand, for the gas (a proxy for DM caustics) at very high z for lower mass galaxies (again not very far from linear dynamics at this epoch). Hence, we found in both regimes that some imprint of the LSS geometry and dynamics is directly responsible for the spin of the forming object and its post-merger transition. In this paper, we tried and explained the origin of the statistical signal, but we do not argue that large-scale dynamics dominate the non-linear regime of galaxy evolution on an individual object basis.

The remaining task involves understanding in detail the redshift dependence of the transition masses $M_{\rm crit}$ described by equations (1) and (2) [and also its dependence on the smoothing length, which might allow us to identify a scale at which the (anti-)alignment is strongest]. It would also clearly be of interest to further quantify (using larger samples) the findings of Hahn et al. (2010) regarding the alignment of the stellar disc/circumgalactic medium with respect to the LSS and investigate how these results depend on subgrid physics and feedback processes.

Let us conclude this paper with some speculations about what these results imply specifically for the process of galaxy formation at high redshift.

4.2 Implications for galaxy formation

We are now in a position to *speculate* about the implication of our findings for high-redshift galaxy formation. In the view of the robust measurements of Section 2 and Appendix A and the visual inspections of Section 3, it appears that (i) galaxies form preferentially along filaments; and (ii) their internal dynamics (hence their morphology) inherit important features from this anisotropic environment. The first point is backed by the distribution of filaments at the virial radius (appendix A of Pichon et al. 2011; Danovich et al. 2012, and indirectly by Fig. 1) and the second point by the measurements reported in this paper.

Indeed, filaments can be thought of as loci of constructive interferences from the long-wavelength modes of the initial power spectrum. On top of these modes, constructive interferences of high-frequency modes produce peaks which thus get a boost in density that allows them to pass the critical threshold necessary to decouple from the overall expansion of the Universe, as envisioned in the spherical collapse model (Gunn & Gott 1972). This well-known biased clustering effect has been invoked to justify the clustering of galaxies around the nodes of the cosmic web (White, Tully & Davis 1988). It also explains why galaxies form in filaments. In walls alone, the actual density boost is not sufficiently large to trigger galaxy formation. We therefore argue here that, statistically, the main nodes of the cosmic web are where galaxies migrate, not where they form; galaxies generally form while reaching filaments from walls. They thus inherit the anisotropy of their birth place as spin orientation. During migration, they may collide with other galaxies/haloes and erase part of their birth heritage when converting orbital momentum into spin via merger.

Recently, Pichon et al. (2011) showed how the cold gas drains out of the prominent voids in the cosmic web into sheets and filaments before it finally gets accreted on to DM haloes. Interestingly, the imprint of the larger scale pancake structure of the typical cosmic web around a filament and a peak allows us to be more specific about the geometry of this process. Indeed, one of the striking features of Figs 8 and 9 (probably best seen in the animation available as Supporting Information with the online version of the paper) is those ribbon-like caustics which feed the central galaxy along its spin axis from both poles. Generically, the gas inflow in the frame of the galaxy is double-helix like along its spin axis; this is mostly wiped out in DM (and hardly visible in Fig. 1) because of shell crossing, but quite visible for the gas. These ribbons are generated via the same winding/folding process as for the protogalaxy, and represent the dominant source of secondary filamentary infall described in Pichon et al. (2011), which feeds the newly formed galaxy with gas of well-aligned angular momentum (whose direction was set by the impact parameter offset of the two neighbouring walls, which can in turn be attributed to the dissymmetry of the four neighbouring voids). As such, the larger scale geometry of the LSS (which biases the formation process) squashes the average neighbourhood of a peak (six saddles, eight voids, twelve walls) into a simpler effective geometry (one wall and one embedded filament dominating). Formally, the most likely 'crystal' of the Universe – subject to the constraint of collapse along two axes on larger scales – differs from the azimuthally averaged cubic centred crystal found in Pichon et al. (in preparation): it is quite flattened and dominated by one ridge (Pichon et al. 2011; Danovich et al. 2012; Dubois et al. 2012). Note that the gas flowing roughly parallel to the spin axis of the disc along both directions will typically impact the disc's circumgalactic medium and shock once more (as it did when it first reached the wall, and then the filaments, forming those above-mentioned ribbons), radiating away its vertical momentum (see Fig. 10 and Tillson, Miller & Devriendt 2011).

Our speculations here have focused on a two-scale process. Given the characteristics of ΛCDM hierarchical clustering, one can anticipate that this process occurs on several nested scales at various epochs – and arguably on various scales at the same epoch.[3] In other words, one expects smaller scale filaments are themselves embedded in larger scale walls (as discussed in Appendix A to reconcile our excess alignment with the eigenvectors of the tidal tensor). The induced multiscale anisotropic flow transpires in the scaling of transition mass with the smoothing length, as discussed in Appendix D1.

Another issue would be to estimate for how long this entanglement between the large-scale dynamics and the kinematic properties of high redshift pervades. Indeed, Ocvirk, Pichon & Teyssier (2008)

[2] Note, however, that such a typical caustic should have inherited some level of asymmetry (Pichon et al. 2011), which could imply that one vortex dominates.

[3] The scenario we propose for the origin of this signal is, like the signal itself, relative to the linear scale involved in defining the filaments and, as such, multiscale. It will hold as long as filaments are well defined in order to drive the local cosmic flow.

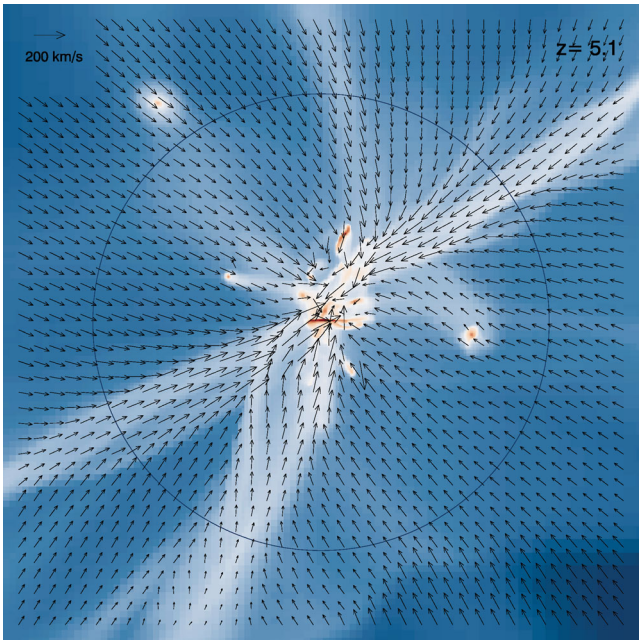

Figure 10. A meridional projection through the velocity flow and gas density around the NUT galaxy at redshift 5.1 (Kimm et al. 2011). The disc plane is along the horizontal axis and the circle marks the virial radius (17.6 kpc). Note the ribbon-like cold flows seen directly in the gas density and the velocity flow, which hit the galactic disc roughly along its spin axis. Note also how the gas takes a sharp turn when it reaches the ribbons.

have shown that at lower redshift the so-called hot mode of accretion will kick in; how will hot flows wash out/disintegrate these ribbons? Given that they locally reflect the large-scale geometry, will the gas continue to flow in along preferred directions (as DM does, see e.g. Aubert, Pichon & Colombi 2004), or does the hot phase erase any anisotropy? Will the above-mentioned smaller scale non-linear dynamics eventually wash out any such trace?

Finally, note that the actual spin of the stellar disc at low redshift need not be trivially related to that of its larger scale gravitational patch (see, for instance, Hahn et al. 2010), as a significant amount of angular momentum redistribution takes place in the circumgalactic medium (Kimm et al. 2011) over cosmic time.

ACKNOWLEDGMENTS

We thank J. Binney, M. Haehnelt, S. Peirani, S. Prunet and T. Kimm for advice, and our collaborators of the Horizon Project (www.projet-horizon.fr) for helping us produce the Horizon 4π simulation. We also thank the anonymous referee for constructive criticism. The hydrodynamical simulation presented here was run on the DiRAC facility jointly funded by STFC, the Large Facilities Capital Fund of BIS and the University of Oxford. CP acknowledges support from a Leverhulme visiting professorship at the Department of Physics of the University of Oxford, and thanks the Merton College, Oxford, for a visiting fellowship. DP thanks the French Canada Research Fund and the University of Oxford. JD and AS's research is supported by Adrian Beecroft, the Oxford Martin School and STFC. Special thanks to T. Kimm for Fig. 10, F. Bouchet for allowing us to use the Magique 3 supercomputer during commissioning, and to S. Rouberol for making it possible. We also thank D. Munro for freely distributing his YORICK programming language and OPENGL interface (available at http://yorick.sourceforge.net/).

REFERENCES

Aragón-Calvo M. A., van de Weygaert R., Jones B. J. T., van der Hulst J. M., 2007, ApJ, 655, L5
Aubert D., Pichon C., Colombi S., 2004, MNRAS, 352, 376
Bailin J., Steinmetz M., 2005, ApJ, 627, 647
Barrow J. D., Bhavsar S. P., Sonoda D. H., 1985, MNRAS, 216, 17
Bond J. R., Myers S. T., 1996, ApJS, 103, 1
Bond J. R., Kofman L., Pogosyan D., 1996, Nat, 380, 603
Bond N. A., Strauss M. A., Cen R., 2010, MNRAS, 409, 156
Catelan P., Theuns T., 1996, MNRAS, 282, 436
Crittenden R., Natarajan P., Pen U., Theuns T., 2001, ApJ, 559, 552
Danovich M., Dekel A., Hahn O., Teyssier R., 2012, MNRAS, 422, 1732
Davis M., Efstathiou G., Frenk C. S., White S. D. M., 1985, ApJ, 292, 371
Dekel A., 1985, ApJ, 298, 461
Desjacques V., 2008, MNRAS, 388, 638
Doroshkevich A. G., 1970, Astrofizika, 6, 581
Dubois Y., Teyssier R., 2008, A&A, 477, 79
Dubois Y., Pichon C., Haehnelt M., Kimm T., Slyz A., Devriendt J., Pogosyan D., 2012, MNRAS, 423, 3616
Faltenbacher A., Gottlöber S., Kerscher M., Müller V., 2002, A&A, 395, 1
Flin P., Godlowski W., 1986, MNRAS, 222, 525
Flin P., Godlowski W., 1990, Sov. Astron. Lett., 16, 209
Forero-Romero J. E., Hoffman Y., Gottlöber S., Klypin A., Yepes G., 2009, MNRAS, 396, 1815
Godłowski W., Flin P., 2010, ApJ, 708, 920
González R. E., Padilla N. D., 2010, MNRAS, 407, 1449
Gunn J. E., Gott J. R., III, 1972, ApJ, 176, 1
Haardt F., Madau P., 1996, ApJ, 461, 20
Hahn O., Porciani C., Carollo C. M., Dekel A., 2007a, MNRAS, 375, 489
Hahn O., Carollo C. M., Porciani C., Dekel A., 2007b, MNRAS, 381, 41
Hahn O., Teyssier R., Carollo C. M., 2010, MNRAS, 405, 274
Hatton S., Ninin S., 2001, MNRAS, 322, 576
Hoyle F., 1949, in Burgers J. M., van de Hulst H. C., eds, Problems of Cosmical Aerodynamics. Central Air Documents Office, Dayton, OH, p. 195
Huchra J. P., Geller M. J., 1982, ApJ, 257, 423
Icke V., 1973, A&A, 27, 1
Kimm T., Devriendt J., Slyz A., Pichon C., Kassin S. A., Dubois Y., 2011, preprint (arXiv:e-prints)
Komatsu E. et al., 2011, ApJS, 192, 18
Lee J., Erdogdu P., 2007, ApJ, 671, 1248
Lee J., Pen U., 2000, ApJ, 532, L5
Lee J., Pen U.-L., 2002, ApJ, 567, L111
Lemson G., 1993, MNRAS, 263, 913
Libeskind N. I., Hoffman Y., Knebe A., Steinmetz M., Gottlöber S., Metuki O., Yepes G., 2012, MNRAS, 421, L137
Lynden-Bell D., 1964, ApJ, 139, 1195
Navarro J. F., Abadi M. G., Steinmetz M., 2004, ApJ, 613, L41
Novikov D., Colombi S., Doré O., 2006, MNRAS, 366
Ocvirk P., Pichon C., Teyssier R., 2008, MNRAS, 390, 1326
Paz D. J., Stasyszyn F., Padilla N. D., 2008, MNRAS, 389, 1127P
Peebles P. J. E., 1969, ApJ, 543, L107
Peebles P. J. E., 1980, The Large-Scale Structure of the Universe. Princeton Univ. Press, Princeton, NJ
Peirani S., Mohayaee R., de Freitas Pacheco J. A., 2004, MNRAS, 348, 921
Pichon C., Bernardeau F., 1999, A&A, 343, 663
Pichon C., Pogosyan D., Kimm T., Slyz A., Devriendt J., Dubois Y., 2011, MNRAS, 418, 2493
Platen E., van de Weygaert R., Jones B. J. T., 2007, MNRAS, 380, 551
Platen E., van de Weygaert R., Jones B. J. T., 2008, MNRAS, 387, 128
Pogosyan D., Bond J. R., Kofman L., Wadsley J., 1998, in Colombi S., Mellier Y., Raban B., eds, Wide Field Surveys in Cosmology Cosmic Web: Origin and Observables. Editions Frontières, Gif-sur-Yvette, p. 61
Pogosyan D., Pichon C., Gay C., Prunet S., Cardoso J. F., Sousbie T., Colombi S., 2009, MNRAS, 396, 635
Porciani C., Dekel A., Hoffman Y., 2002, MNRAS, 332, 325

Prunet S., Pichon C., Aubert D., Pogosyan D., Teyssier R., Gottloeber S., 2008, ApJS, 178, 179
Rasera Y., Teyssier R., 2006, A&A, 445, 1
Schäfer B. M., 2009, Int. J. Mod. Phys. D, 18, 173
Sheth R. K., Mo H. J., Tormen G., 2001, MNRAS, 323, 1
Slosar A., White M., 2009, J. Cosmol. Astropart. Phys., 6, 9
Sousbie T., 2011, MNRAS, 414, 350
Sousbie T., Pichon C., Colombi S., Novikov D., Pogosyan D., 2008, MNRAS, 383, 1655
Sousbie T., Colombi S., Pichon C., 2009, MNRAS, 393, 457
Spergel D. N. et al., 2003, ApJS, 148, 175
Stoica R. S., Martìnez V. J., Mateu J., Saar E., 2005, A&A, 434, 423
Sugerman B., Summers F. J., Kamionkowski M., 2000, MNRAS, 311, 762
Sutherland R. S., Dopita M. A., 1993, ApJS, 88, 253
Teyssier R., 2002, A&A, 385, 337
Teyssier R. et al., 2009, A&A, 497, 335
Tillson H., Miller L., Devriendt J., 2011, MNRAS, 417, 666
Trujillo I., Carretero C., Patiri S. G., 2006, ApJ, 640, L111
Tweed D., Devriendt J., Blaizot J., Colombi S., Slyz A., 2009, A&A, 506, 647
Varela J., Betancort-Rijo J., Trujillo I., Ricciardelli E., 2012, ApJ, 744, 82
White S. D. M., 1984, ApJ, 286, 38
White S. D. M., Silk J., 1979, ApJ, 231, 1
White S. D. M., Tully R. B., Davis M., 1988, ApJ, 333, L45
Zel'Dovich Y. B., 1970, A&A, 5, 84
Zeldovich I. B., Einasto J., Shandarin S. F., 1982, Nat, 300, 407
Zhang Y., Yang X., Faltenbacher A., Springel V., Lin W., Wang H., 2009, ApJ, 706, 747

APPENDIX A: SPIN–TIDAL TENSOR CORRELATIONS

Let us present a complementary set of measurements: the correlations between the spin axis of dark haloes and the orientation of the large-scale gravitational tidal tensor $T_{ij} = \partial_{ij}\phi - \frac{1}{3}\Delta\phi\delta_{ij}$. To describe the orientation of the tidal tensor, we define $\boldsymbol{e}_1$, $\boldsymbol{e}_2$ and $\boldsymbol{e}_3$ to be the minor, intermediate and major eigendirections of T_{ij} according to the sorted eigenvalues $\lambda_1 \leq \lambda_2 \leq \lambda_3$ of the Hessian of the gravitational potential, $\partial_{ij}\phi$ (with which the tidal tensor shares the eigendirections).

Besides works based on the correlations between spin orientation and the cosmic web described in the main text (Section 1), the only numerical study to date looking at the alignment between halo spin and tidal tensor was done by Porciani, Dekel & Hoffman (2002) who predicted its orthogonality with the major principal axis but also found that galactic spins must have lost their initial alignment with the tidal tensor predicted by TTT. Direct observations of the alignment between the spin and the tidal tensor eigenvectors have also been carried out: the first attempt by Lee & Pen (2002) studied the correlations between the disc orientation of the galaxies from the Tully catalogue and the shear reconstructed from the Point Source Catalog Redshift Survey and rejected the hypothesis of randomness at a 99.98 per cent confidence level. More recently, Lee & Erdogdu (2007) detected some correlations between the spin and the intermediate eigenvector of the tidal tensor and found that galactic spins were also preferentially perpendicular to the major principal axis but this signal remains weak. To overcome this lack of a clear numerical detection, the use of the 43 million halo sample of the Horizon 4π simulation presents a tremendous advantage, as it allows us to very robustly calculate the correlations between halo spin orientation and the local tidal tensor. We show in this appendix that these measurements are not only consistent with the spin–filament correlations, but actually lend additional support to the interpretation of this paper in terms of large-scale dynamics along walls and filaments.

At the onset of non-linearity, the gravitational potential tracks the velocity potential of the matter flow. Thus, the signs of λ_i determine whether the flow in the corresponding direction compresses ($\lambda_i > 0$) or rarifies ($\lambda_i < 0$) matter. At a given smoothing scale, this criterion can be used to partition space into peak-like $0 < \lambda_1 \leq \lambda_2 \leq \lambda_3$, filament-like $\lambda_1 < 0$, $0 < \lambda_2 \leq \lambda_3$, wall-like $\lambda_1 \leq \lambda_2 < 0$, $0 < \lambda_3$ or void-like $\lambda_1 \leq \lambda_2 \leq \lambda_3 \leq 0$ regions (Pogosyan et al. 1998). From this point of view, in the peak regions matter compression is strongest along $\boldsymbol{e}_3$ and weakest along $\boldsymbol{e}_1$. In the filamentary regions, $\boldsymbol{e}_1$ gives the direction of the filament, while the walls are collapsing along $\boldsymbol{e}_3$ and extend, locally, in the plane spanned by $\boldsymbol{e}_1$ and $\boldsymbol{e}_2$.

At this stage, it is important to note that the tidal field probes larger scale structures than the filamentary structure studied in Section 3 as the gravitational potential is a smoother version of the density field (through Poisson's equation). In other words, the Skeleton of the potential (which locally corresponds to the eigendirections of the tidal tensor) traces the cosmic structures (walls, filaments, etc.) on scales much larger than the Skeleton of the density. Thus, if we turn to a formulation in terms of the Skeleton of the potential, the filaments described in Section 3 are embedded in the large-scale walls of the potential field (as illustrated in Fig. A1); therefore, protogalaxy formation begins with the first collapse (namely the collapse of $\boldsymbol{e}_3$) leading to the formation of the large-scale walls because it corresponds on smaller scale to the time when the filaments (of the density field) form by winding.

Note that a stricter definition of a filament in the local theory of the Skeleton (Sousbie et al. 2008) as a ridge in the density profile associates its local direction with the minor eigendirection of the Hessian of the *density* (here, to match enumeration, taken with a negative sign) $\boldsymbol{e}_1^{\rho}$. Thus, as the potential is two derivatives away from the density, the excess probability of alignment between the

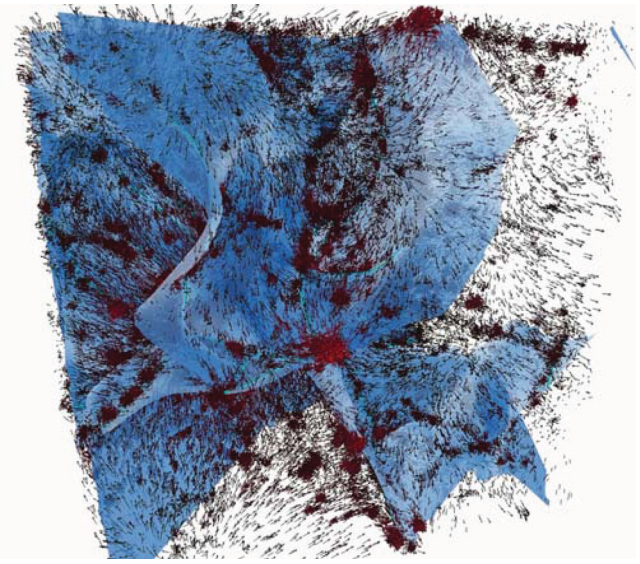

Figure A1. The walls of the potential (in blue) and its filaments (in cyan), together with the velocities of DM particles (in red) of a $20\,h^{-1}$ Mpc 512^3 DM particle ΛCDM simulation with *WMAP1* cosmogony. At redshift zero, most DM haloes sit in these walls, while the velocity field empties the voids and flows within those walls. This divergent flow is best seen in the top (hence bottom) left-hand void (see also the animations available as Supporting Information with the online version of the paper).

halo spin and $\boldsymbol{e}_1$ should be quite similar to that of the alignment between the halo spin and the filament's direction.

A1 Alignment between spin and tidal eigendirections

In order to compute the excess probability of alignment between the spin of DM haloes and the eigenvectors of the tidal tensor, the density field is again smoothed over $5\,h^{-1}$ Mpc (for $z = 0$), Poisson's equation is solved via fast Fourier transform in smaller overlapping boxes (boundary effects are found to be insignificant inside the boxes), the Hessian matrix of the potential is computed using a finite difference scheme and this matrix is finally interpolated to halo positions. We then measure the angle between the angular momentum vector of the halo and each eigendirection of the tidal tensor and compute the histogram of the absolute value of the cosine of this angle; after normalization, it gives $1 + \xi$, the excess probability of alignment between the spin and the tidal tensor eigendirections. As in Section 2.2, the data are then split by halo mass.

Fig. A2 displays these excess probabilities in three panels corresponding to the orientation of the spin with respect to $\boldsymbol{e}_1$, $\boldsymbol{e}_2$ and $\boldsymbol{e}_3$ (top, middle and bottom panels, respectively), at $z = 0$. Haloes of all masses have spins that preferentially avoid the direction of the strongest large-scale compression, $\boldsymbol{e}_3$, at 10 per cent excess probability (bottom panel). The exception is the very highest mass bin, which shows an additional halo population with spins aligned with $\boldsymbol{e}_3$.

For the high-mass, $M > M_0^{\rm t} \approx 8(\pm 2) \times 10^{12}\,{\rm M}_\odot$, haloes we detect a strong trend for the spin to be aligned with $\boldsymbol{e}_2$, the intermediate principal axis of the tidal tensor with an excess probability of up to 40 per cent (blue and green lines, middle panel), and to be perpendicular to the minor, $\boldsymbol{e}_1$, principal axis with an excess probability of up to 20 per cent (blue and green lines, top panel), a result in agreement with Lee & Erdogdu (2007) and Porciani et al. (2002).

Spins of the lower mass, $M < M_0^{\rm t}$, haloes tend, in contrast, to align with $\boldsymbol{e}_1$ (red and orange lines, top panel), thus preferring the direction of the filamentary structures $\boldsymbol{e}_1$, with an excess probability of up to 15 per cent, and in a weaker way to align with $\boldsymbol{e}_2$ (with an excess probability of 5 per cent, see the red and orange lines in the middle panel).

These results are in exact agreement with our findings using the Skeleton that the spins of sufficiently large haloes prefer to be perpendicular to the filament's direction, while small haloes show a positive correlation for a spin orientation along the filaments. Indeed, the bottom panel of Fig. A2 is almost identical to the spin–filament correlation found in Fig. 3. For the tidal tensor, the transition occurs at a somewhat higher mass, $M_0^{\rm t} \approx 8 \times 10^{12}\,{\rm M}_\odot$, than for the Skeleton probe. This is not surprising because of the effectively larger scales probed by the tidal tensor and the observation (see Section 2.2 and Appendix D1) that the critical mass increases with the smoothing length used to define the LSS.

The redshift dependence of the transition mass was also investigated (as described in the main text, see Section 2.3) and is found to be

$$M_{\rm crit}^{\rm t} \approx M_0^{\rm t}(1+z)^{-\gamma_{\rm t}}, \quad \gamma_{\rm t} = 3 \pm 0.3, \quad M_0^{\rm t} \simeq 8(\pm 2) \times 10^{12}\,{\rm M}_\odot.$$

A2 Consistency with LSS cosmic flows

Let us describe this spin acquisition in the framework of large-scale dynamics and the ellipsoidal collapse model (Lynden-Bell 1964; Zel'Dovich 1970; Icke 1973; White & Silk 1979; Peebles 1980;

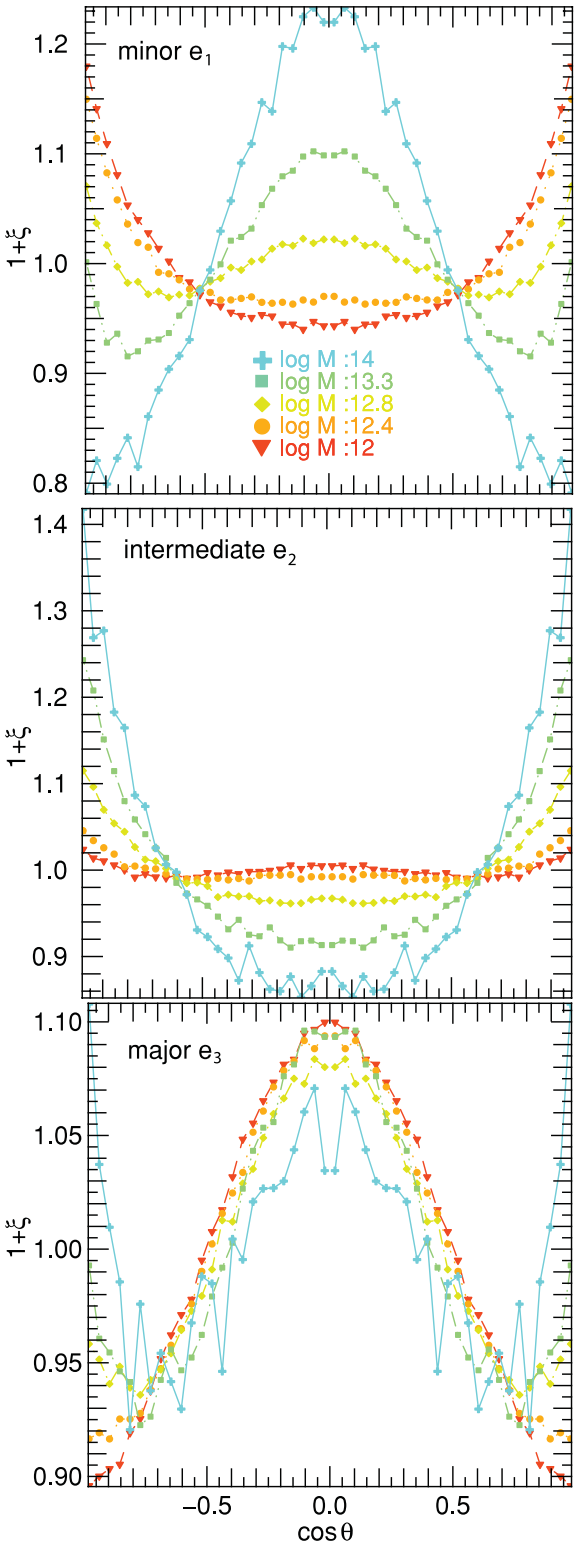

Figure A2. Excess probability of alignment between the spin and the minor/intermediate/major axis (from the top to bottom) of the tidal tensor in the Horizon 4π simulation. Different mass bins are colour-coded from 10^{12} (red) to $10^{14}\,{\rm M}_\odot$ (blue). A transition is detected: the spin of high-mass haloes tends to be aligned with the intermediate principal axis (middle panel), whereas the spin of low-mass haloes tends more likely to point along the minor axis (top panel).

Lemson 1993; Bond & Myers 1996; Sheth, Mo & Tormen 2001; Desjacques 2008, among others). Low-mass haloes form by accretion at high redshift. At this time, sheets and filaments are forming by the successive collapse of $\boldsymbol{e}_3$ and $\boldsymbol{e}_2$, respectively. When $\boldsymbol{e}_3$ is collapsing, low-mass haloes form by accreting particles whose motion is along the direction $\boldsymbol{e}_3$. This process induces a spin perpendicular to this direction, that is, in the plane $(\boldsymbol{e}_1, \boldsymbol{e}_2)$ which is the plane of the large-scale wall in which they are located. Then, $\boldsymbol{e}_2$ begins to collapse and other low-mass haloes form from objects moving in the plane $(\boldsymbol{e}_2, \boldsymbol{e}_3)$, thus acquiring a spin perpendicular to this plane, that is, aligned with $\boldsymbol{e}_1$ (which is the direction of the forming large-scale filament). The first generation of DM haloes (of typically low mass) are now formed; as mentioned in Section 3, for low-mass haloes at redshift zero, the spin will not change much as they have already acquired most of their mass. Fig. 6 (left-hand panel) provides a clear illustration for this: a low-mass halo forms and acquires a spin aligned with $\boldsymbol{e}_1$ as expected. It has been pointed out above that halo spin orientation must be either aligned with $\boldsymbol{e}_1$ (correlated to the filament's direction), or in the plane $(\boldsymbol{e}_1, \boldsymbol{e}_2)$ depending on the time when they form. This is in good agreement with the top and middle panels of Fig. A2 which show an excess probability for their spin to be aligned with $\boldsymbol{e}_1$ (or with the filaments) and in a weaker way with $\boldsymbol{e}_2$ (see the red and orange lines which represent the low-mass haloes at redshift zero, that is, the haloes with a mass between 3×10^{11} and $3 \times 10^{12}\,\mathrm{M}_\odot$).

Later (as described in Section 3 in terms of flows along the filaments), $\boldsymbol{e}_1$ collapses and the haloes located in the filaments of the potential stream along this direction. Most of the more massive haloes then form by mergers in this flow and therefore acquire a spin which combines the spin of their progenitors and the orbital spin provided by the merger. The orbital spin must be in the plane perpendicular to $\boldsymbol{e}_1$, that is, $(\boldsymbol{e}_2, \boldsymbol{e}_3)$ because the progenitors move along the filaments before merging, whereas the spin of their (less massive) progenitors is in the plane $(\boldsymbol{e}_1, \boldsymbol{e}_2)$. The resulting angular momentum is therefore a superposition of these various spins, statistically more likely to be aligned with $\boldsymbol{e}_2$, which is what shown in Fig. 6 (right-hand panel) and which is also in good agreement with the middle panel of Fig. A2, where the blue and green lines representing haloes above $2 \times 10^{13}\,\mathrm{M}_\odot$ reveal a strong trend for these high-mass haloes to be aligned with $\boldsymbol{e}_2$. For these massive DM haloes, the competition between the orbital spin and the intrinsic spin during the merger process was already pointed out in Section 3. The excess probability for their spin to be aligned with $\boldsymbol{e}_2$ suggests that neither one nor the other dominates. Nevertheless, very massive haloes (with masses above $10^{14}\,\mathrm{M}_\odot$) represented with a blue line in Fig. A2 seem to have their spin less perpendicular to $\boldsymbol{e}_3$: actually we can observe two modes, one perpendicular and one aligned with this direction, which can be understood if they are the result of a further generation of mergers whose intrinsic spins were already perpendicular to the filament.

Let us emphasize that this explanation and that which was presented in Section 3 are consistent. Indeed, in Section 3 our claim is that the winding of the walls is responsible for the direction of the spin of low-mass haloes. Meanwhile, in this appendix, the focus is on the first collapse along $\boldsymbol{e}_3$, that is, on the formation of walls. However, as pointed out in the introduction of this appendix, the tidal field probes *larger* scale structures than the filaments of the density field studied in Section 3. Taking into account this difference, it turns out that the two analyses are complementary (describing the large-scale dynamics on different scales). It also helps reconciling the findings of Porciani et al. (2002) and Lee & Erdogdu (2007) which rely on the tidal tensor with those of Bailin & Steinmetz (2005), Aragón-Calvo et al. (2007), Hahn et al. (2007b) and Paz et al. (2008) which involve the density field filamentary structure.

APPENDIX B: CIRCUMGALACTIC MEDIUM SPIN

Let us first describe briefly the *hydrodynamical* simulation that we will use to assess the alignment of the gas component surrounding the galaxies with the large-scale filamentary structure. This simulation is described in more details in Dubois et al. (2012) and corresponds to their SHhr run. Let us recall here its basic properties. The SHhr simulation follows the formation of a massive ($M_{\rm vir} = 5 \times 10^{11}\,\mathrm{M}_\odot$ at $z = 6$) halo within a resimulated region in a $100\,h^{-1}$ Mpc box size, its DM mass resolution is $1.3 \times 10^6\,\mathrm{M}_\odot$, and minimum cell size is 17 pc. The cosmology employed in that run is slightly different from the parameters of the Horizon 4π simulation, and is compatible with the *WMAP7* cosmology (Komatsu et al. 2011): $\Omega_{\rm m} = 0.27$, $\Omega_\Lambda = 0.73$, $\Omega_{\rm b} = 0.045$, $H_0 = 70\,\mathrm{km\,s^{-1}\,Mpc^{-1}}$, $n = 0.961$ and $\sigma_8 = 0.8$. The gas is allowed to cool down radiatively down to $T_0 = 100\,\mathrm{K}$, assuming an initial metal enrichment of $10^{-3}\,\mathrm{Z}_\odot$ (Sutherland & Dopita 1993). An ultraviolet background heating source term is added to the gas energy equation following Haardt & Madau (1996) with reionization taking place at $z_{\rm reion} = 8.5$. Star formation is allowed in gas density regions above $n_0 = 50\,\mathrm{H\,cm^{-3}}$ using a Poisson random process (Rasera & Teyssier 2006; Dubois & Teyssier 2008) that reproduces the Schmidt–Kennicutt law $\dot{\rho}_* = \epsilon_* \rho / t_{\rm ff}$, where $\dot{\rho}_*$ is the star formation rate density, $\epsilon_* = 0.01$ is the star formation efficiency and $t_{\rm ff}$ is the local free-fall time of the gas with local density ρ. No feedback from supernovae or active galactic nuclei is accounted for. Tracer particles that passively follow the motion of the gas are scattered in the initial conditions and allow us to trace back the Lagrangian trajectories of gas elements that end up in collapsed structures.

Fig. B1 displays two large-scale views of this hydrodynamical simulation and its tracer particles at redshift 9 shown in Fig. 8. Structures and substructures in DM are detected with the Most massive Sub-node Method (Tweed et al. 2009) and only masses above $5 \times 10^8\,\mathrm{M}_\odot$ are selected. The spin of the circumgalactic medium (accounting for non-star-forming gas only with gas density below $n_{\rm H} < 50\,\mathrm{H\,cm^{-3}}$) between 0.1 and $0.25 R_{\rm vir}$ is then computed and its orientation is represented with the dark red segments. This somewhat ad hoc criterion used to define the spin reflects our focus on the angular momentum of the secondary infall gas, which has just been or is being accreted; our measurements correspond to an average of the spin within this subregion of the DM halo. This figure shows a good alignment of the spins with the circumgalactic polar filaments (i.e. the filament which visually flows along the polar axis of the galaxy, in particular for clumps 2, 3, 4 and 5). This is consistent with visual inspection (Fig. 8, but best viewed via the online Supporting Information) and with the prediction of Fig. 3, since the critical mass at that redshift is $6 \times 10^{10}\,\mathrm{M}_\odot$. The spin of a couple of low-mass clumps in that field (noticeably clumps 1 and 6) is in fact poorly estimated automatically, as the DM clump centre can be offset at that redshift relative to that of the circumgalactic disc.

APPENDIX C: ROBUSTNESS OF THE SPIN–FILAMENT CORRELATION

Let us assess how robust the spin orientation–filament correlation found in Section 2.2 is by carrying out a few consistency tests.

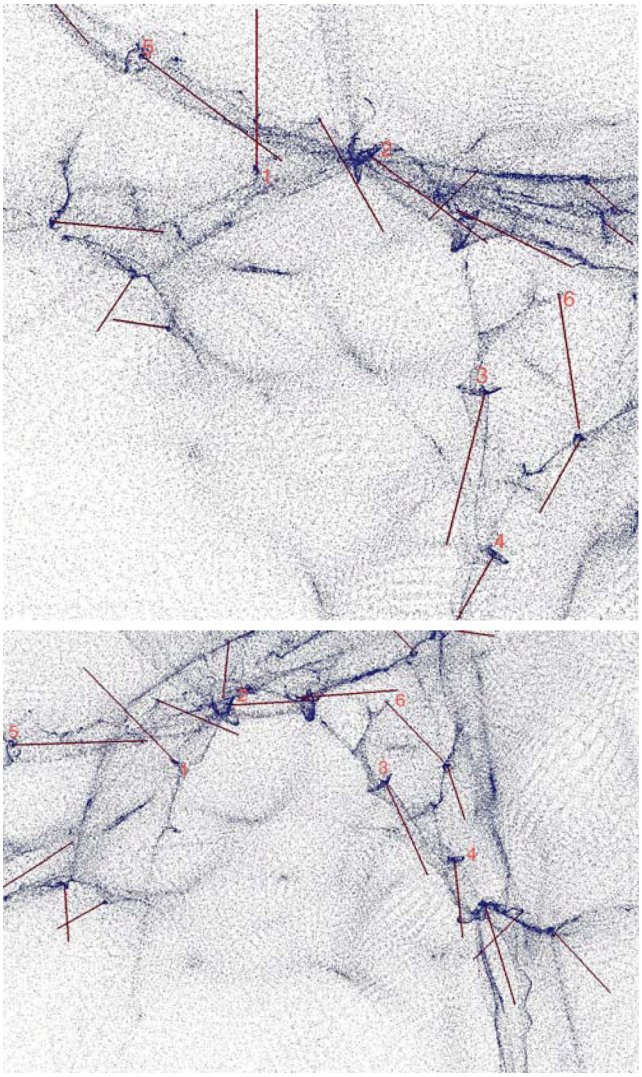

Figure B1. Distribution of hydrodynamical tracer particles (in blue) at redshift 9 along two different viewing angles. The spin direction of the circumgalactic medium between 0.1 and $0.25R_{\rm vir}$ of some protogalaxies is plotted in red. On average the spins are more likely to be aligned with the filaments (as seen with protogalaxies 2, 3, 4 and 5, for example).

In order to check the effect of mass resolution (the spin of very low mass haloes is poorly defined, for instance, as too few particles are involved in its measurement), the same measurements are carried out in a smaller simulation (256^3 particles in a $50\,h^{-1}$ Mpc periodic box with the same cosmology) for which same physical masses are represented by higher numbers of particles: mass bins from 3×10^{11} (red) to $6 \times 10^{12}\,{\rm M}_\odot$ (green) correspond to 30–1400 particles in Horizon 4π (corresponding to a lower threshold for the FoF detection) since the mass per particle is $7 \times 10^9\,{\rm M}_\odot$; in contrast, 350–15 000 particles are found in haloes of the same mass for the small simulation since the mass per particle is $6 \times 10^8\,{\rm M}_\odot$. The detection of the same phase transition (see Fig. C1) occurring at the same halo mass demonstrates that the signal is not induced by limited mass resolution. This result is also consistent with the findings of Aragón-Calvo et al. (2007) and Hahn et al. (2007b).

Another simple check involves varying the procedure by choosing for each halo the closest segments of the Skeleton (instead of for each segment, the closest haloes). The signal we get is very similar to Fig. 3 (low-mass haloes tend to be parallel to the filaments with

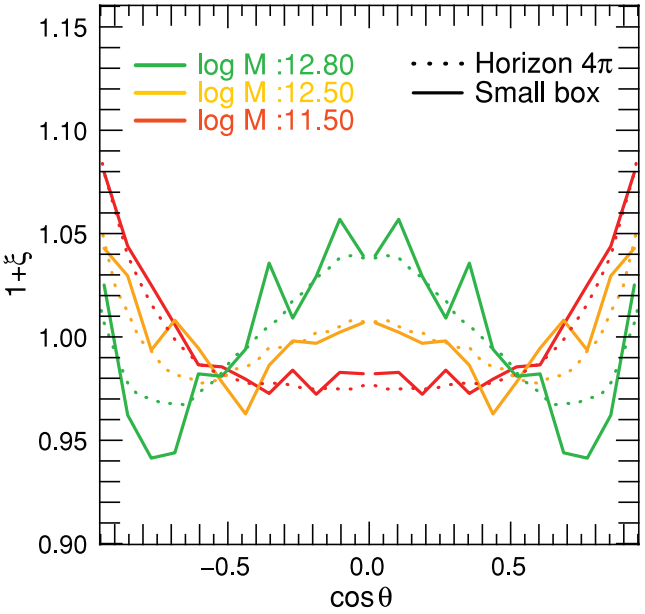

Figure C1. Excess probability of spin–filament alignment in various simulations. Measurements in the Horizon 4π simulation are plotted with the dotted lines and measurements in the smaller simulations are plotted with the solid lines. Different colours correspond to different halo mass bins from 3×10^{11} (red) to $6 \times 10^{12}\,{\rm M}_\odot$ (green). The signal in the Horizon 4π simulation is statistically consistent with that of the smaller simulations.

an excess probability of 15 per cent and high-mass haloes perpendicular with an excess probability reaching 20 per cent for the more massive bin which is even stronger than in Fig. 3), suggesting that the measured correlations are independent of the detailed procedure implemented to identify neighbours.

Haloes at the nodes of the Skeleton cannot have a well-defined closest segment direction, as more than one Skeleton segment typically qualifies, and could therefore bias our measurements. So as to quantify this effect, the same algorithm is implemented but with a new criterion: haloes closer than a certain distance to the nodes are not considered. An even stronger signal is detected, which leads us to conclude that nodes introduce extra noise and are not the cause for the observed signal.

One might also think this result could depend on a density threshold for the underlying filament. Hence, the same data in low-, intermediate- and high-density filaments were plotted: the excess probability of spin–filament alignment is found to be the same whatever the density inside the filaments is. All these tests demonstrate the overall robustness of the mass-dependent transition of the relative alignment.

APPENDIX D: CHARACTERISTIC MASSES

In the main text, the density field was smoothed over a scale of $5\,h^{-1}$ Mpc corresponding to a mass of $1.9 \times 10^{14}\,{\rm M}_\odot$. The transition mass found in Section 2.2 is therefore defined relatively to this mass. In the context of hierarchical clustering, as long as the field is smoothed on scales where filaments are still well defined, one can anticipate some scaling of this transition mass with smoothing. This transition mass should reflect the connection between the geometry of the larger scale flow and the mass scale corresponding to galaxies forming and drifting on this cosmic web.

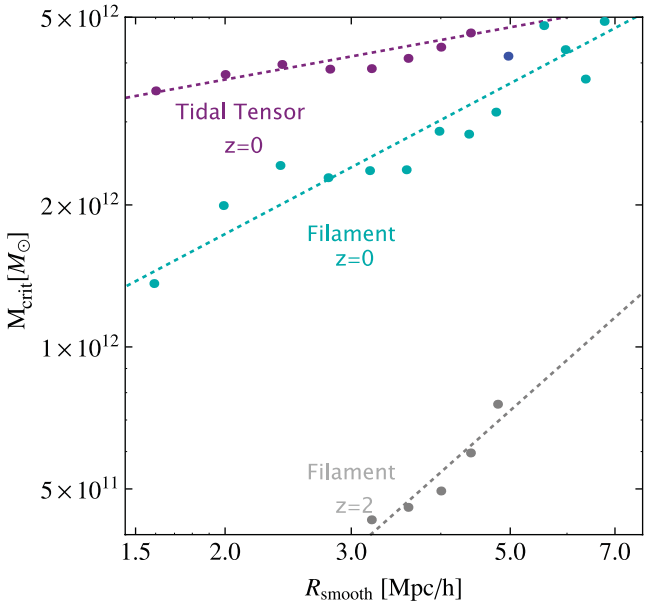

Figure D1. Evolution of the critical mass as a function of the smoothing length for the filaments at redshift zero (cyan) and two (grey) and the tidal tensor at redshift zero (purple). The critical mass increases with the smoothing length with a redshift-dependent slope. The blue dot was measured in the Horizon 4π simulation for the filaments.

D1 Smoothing dependence of the critical mass

Fig. D1 displays the evolution of the critical mass with smoothing length. It is found that $M^{\rm s}_{\rm crit}(R)$ and $M^{\rm t}_{\rm crit}(R)$ can be well fitted by power laws, namely

$$M_0(R) \simeq M_0(R_0) \left(\frac{R}{R_0}\right)^{\alpha}, \qquad \text{(D1)}$$

where $M^{\rm s}_0(R_0) \simeq 3.6(\pm1) \times 10^{12}$, $\alpha^{\rm s} \simeq 0.8 \pm 0.1$, $M^{\rm t}_0(R_0) \simeq 4.8(\pm1)\times10^{12}$ and $\alpha^{\rm t} \simeq 0.28 \pm 0.04$. This scaling is not inconsistent with the discussion of the origin of the alignment given in Section 3 in as much as a smoothing length defines a set of filaments and therefore picks out a halo mass scale corresponding to the haloes that are flowing/merging along these filaments. Note that in practice the dependence on smoothing is actually rather weak (expressed in terms of mass, we have $M_{\rm crit} \propto M^{0.27}_{\rm smooth}$ for filaments defined via the Skeleton and $M_{\rm crit} \propto M^{0.09}_{\rm smooth}$ if structure anisotropy is described via the shear tensor). Fig. D1 also shows that α depends on redshift. Note that as expected, the critical mass for the tidal tensor matches that of the filaments smoothed on a larger scale ($\simeq 7.5\,h^{-1}$ Mpc instead of 5). This confirms the idea that the potential is close to a smoother version of the density field.

D2 Non-linear mass evolution

It is of interest to compare the transition masses, $M^{\rm s}_{\rm crit}(z)$ and $M^{\rm t}_{\rm crit}(z)$, with the mass scale that tracks the development of non-linearity in structure formation. The variance of the density field smoothed on scale R obeys

$$\sigma^2(R,z) = D(z)^2 \int_0^\infty P(k) W^2(kR)\, {\rm d}^3k, \qquad \text{(D2)}$$

with $P(k)$ the power spectrum, and the top-hat filter defined by $W^2(x) = 9(\sin x/x - \cos x)^2/x^2$. The growth factor $D(z)$ is given by

$$D(z) = \frac{5}{2}\Omega_{\rm m} H_0^2 H(z) \int_z^\infty \frac{(1+z)\,{\rm d}z}{H(z)^3},$$

with $H(z) = H_0\sqrt{\Omega_{\rm m}(1+z)^3 + \Omega_\Lambda}$. Here H_0, $\Omega_{\rm m}$ and Ω_Λ are the Hubble constant, the DM and the dark energy density parameters at $z = 0$, respectively.

Fixing the level of (non-)linearity by the condition $\sigma(R(z), z) =$ constant implicitly defines the redshift evolution of the smoothing scale $R(z)$ (expressed in comoving Mpc) that maintains this level of (non-)linearity. This, in turn, corresponds to the mass scale

$$M_{\rm NL}(z) \equiv \frac{4}{3}\pi\bar{\rho} R(z)^3, \qquad \text{(D3)}$$

where $\bar{\rho}$ is the present-day average density of matter in the Universe.

For the matter-dominated CDM Universe with a scale-free power spectrum $P(k) \propto k^n$, $M_{\rm NL}(z) \propto (1+z)^{-6/(n+3)}$. In the Universe with realistic parameters, the redshift dependence of $M_{\rm NL}(z)$ is not a power law, both due to the influence of the Λ term that slows down the growth of the structure at low redshifts, and due to the steepening of the spectrum as one moves to smaller scale at high redshifts.

SUPPORTING INFORMATION

Additional Supporting Information may be found in the online version of this article:

Animations. *Movie1.mov*: a very small subset of skeletons at different redshifts extracted from the Horizon 4π simulation, together with unit vectors showing the orientation of the spin of the corresponding dark matter halo with a mass above the transition mass. The spin is indeed perpendicular to the filament for these massive haloes.
Movie2.mov: time sequence evolution of gas tracer particles trapped in walls and filaments and coalescing to form a central galaxy.
Movie3.mov and Movie4.mov: same as *Movie2.mov* from another projection.
Movie5.mov: gas tracer particles around a forming galaxy; the ribbon-like filamentary structure feeding the central galaxy is clearly visible on this circular view.
Movie6.mov: the time line of a set of tracer particles is shown; each tracer particle is colour coded with a different colour. First the viewer rotates around the large-scale distribution of the time line tracer particle; later only the inner region and late times are shown.
Movie7.mov: tracking in towards a set of filaments, colour coded by tracer particle density at high redshift. The coplanar distribution of filaments is clearly seen, together with young galaxies which tend to sit perpendicular to the filament axes. The cold gas describes ribbons corresponding to the locus of the shocks which feed these young galaxies.
Movie8.mov: same tracking in at some intermediate redshift; some galaxies are in the process of merging.
Movie9.mov: same tracking in at some later redshift; the result of mergers corresponding to galaxies which have a spin perpendicular to the main axes of the filaments.
Movie10.mov: a zoom over the inner region of *Movie7.mov* which illustrates the walls of the large-scale structures, the shock-induced ribbons and a nice example of a galaxy formed with a spin parallel to its filament.

Please note: Wiley-Blackwell are not responsible for the content or functionality of any supporting materials supplied by the authors. Any queries (other than missing material) should be directed to the corresponding author for the article.

This paper has been typeset from a TEX/LATEX file prepared by the author.